Prediction of Reoxidation Inclusion Composition in Casting of Steel

Liang Wang and Christoph Beckermann[1]

Department of Mechanical and Industrial Engineering
The University of Iowa, Iowa City, IA 52242

ABSTRACT

A model is developed to calculate the composition of reoxidation inclusions in steel casting. It is assumed that oxygen is continually absorbed by the steel during pouring. The software package Thermo-Calc is used to obtain the inclusion phase fractions and compositions at a given oxygen content. Both lever rule and Scheil-type analyses are performed. The model is applied to reoxidation of two carbon, one low-alloy, and one high-alloy steel. The effects of variations in the steel composition and the oxygen absorption rate on the inclusion composition are investigated in a parametric study. The mass fraction of absorbed oxygen is determined by matching predicted with previously measured reoxidation inclusion compositions for the various steels. Good agreement is obtained for most phases present in the inclusions. Interestingly, the agreement in the inclusion compositions occurs for all steel grades when the mass fraction of absorbed oxygen is equal to 0.9 wt%. This value is explained using a separate model for the rate of oxygen absorption at the steel-atmosphere interface. Various scenarios are outlined that allow for the 0.9 wt% of absorbed oxygen to be achieved. The model is then used to calculate the amount of alloy elements consumed and inclusions formed as a function of the oxygen boundary layer thickness in the atmosphere and the integrated free surface area of the liquid steel during pouring. It is found that for unprotected liquid steel transfer operations, such as tapping and ladle filling, the integrated free surface area and exposure time product can reach values of the order of 100 m^2s per ton of steel, and that the air-to-steel volume ratio during pouring can be as large as 40. It is concluded that, in order to create a comprehensive tool for simulating reoxidation formation, more detailed models are needed for the external oxygen transfer in the atmosphere, the flow of the liquid steel during pouring, and the internal transport and reactions of chemical species in the steel.

---

[1] Author to whom correspondence should be addressed. Telephone: (319) 335-5681, FAX: (319) 335-5669, E-mail: becker@engineering.uiowa.edu

1 INTRODUCTION

Inclusions are a major cost factor in the production of steel castings. Removing inclusions and refilling the defect areas with weld metal account for approximately 20% of the direct cost of steel castings (Svoboda et al., 1987). Reoxidation inclusions are the most common form of inclusions that are found in steel castings. They account for approximately 83% of the inclusions in carbon and low-alloy steel castings, and approximately 48% of the inclusions in high-alloy and stainless steel castings (Griffin and Bates, 1991). Reoxidation is defined as the reaction of elements in steel with oxygen during pouring of the (deoxidized) steel from the ladle into the mold. Oxygen may come from the surrounding atmosphere, refractories, slag, or the sand mold (Sommerville and McKeogh, 1981). The atmosphere is generally believed to be the primary source of oxygen, and limiting the exposure of the steel to the atmosphere is an important consideration in designing pouring systems.

Large reoxidation inclusions often accumulate on the cope surface of steel castings, where they may be visible to the naked eye. Figure 1a shows an example of the occurrence of such macro-inclusions on the cope surface of two 2.54 cm thick by 25.4 cm wide by 30.5 cm long (1 in. x 10 in. x 12 in.) low-alloy steel experimental plate castings (Carlson and Beckermann, 2004). Here, 0.32 cm (⅛ in.) of material was machined from the cope surface, and the 2.54 cm (1 in.) diameter circles encompass all visible inclusions. Reoxidation inclusions have a particularly detrimental effect on machining and mechanical performance of steel castings, and may cause casting rejection. An image of a typical reoxidation macro-inclusion cut from a low-alloy steel casting is shown in Figure 1b (Griffin and Bates, 1991). The inclusion has a pancake-like shape, with a diameter of about 2 mm, and consists of 34 wt% Al_2O_3, 46 wt% SiO_2, and 20 wt% MnO. The globular shape indicates that at least one of the oxides was in liquid form during formation of the inclusion.

The objective of the present study is to predict the composition of reoxidation inclusions in casting of steels in sand molds. This study is part of a larger project to model the entire process of reoxidation inclusion formation and transport in steel casting (Carlson and Beckermann, 2004). It is shown that the inclusion composition is very sensitive to the steel composition and the amount of oxygen absorbed at the steel-atmosphere interface. Available thermo-chemical analysis software is utilized, which enables parametric studies to be conducted that would be difficult to perform experimentally.

Reoxidation of liquid steel has been investigated extensively in the past (Brabie et al., 1975; Brabie, 1976; Lange and Massard, 1977; Vishkarev and Gorokhov, 1991; Sun and Pehlke, 1995, 1996; Sasai and Mizukami, 1996, 1998, 2000; Goto and Miyazawa, 1998). All of these studies conclude that the oxidation rate is primarily controlled by the rate of oxygen transfer through the atmosphere to the surface of the steel. Only for very low alloy element concentrations, or in the presence of stable oxide layers, do internal diffusion processes become important (Brabie, 1976;

Lange and Massard, 1977; Sun and Pehlke, 1995, 1996; Sasai and Mizukami, 1996). The fact that the oxidation rate is limited by atmospheric transport of oxygen is established in the above references by performing experiments where the O_2 gas partial pressure in the atmosphere is varied. The experiments show that the consumption of oxidizing elements is linearly proportional to the O_2 partial pressure. Only a few studies combine experiments with thermo-chemical modeling to predict the order of the oxidation reactions and the final oxide composition (e.g., Sun and Pehlke, 1995, 1996). The use of thermo-chemical analysis software in modeling oxide inclusion formation has become possible only within the past decade. For example, Hsieh et al. (1996) analyzed inclusion formation in low-alloy steel welds as a function of the weld metal composition using Thermo-Calc (Sundman, 2002). Similarly, Eijk et al. (2000) predicted the evolution of inclusion composition in Ti deoxidized steel. Neither of the latter two studies considered reoxidation, where oxygen is continually transferred to the liquid steel.

The composition and other characteristics of reoxidation inclusions in steel castings have been studied in several projects conducted under the auspices of the Steel Founders' Society of America (SFSA) (Svoboda et al., 1987). Lyman and Boulger (1961) measured inclusion compositions in carbon steel castings as a function of the Al content and the Mn/Si ratio. Griffin and Bates (1986a, 1986b) investigated reoxidation inclusions in both low-alloy and high-alloy steel castings. Extensive use is made of these data in the present study in order to validate the predictions. In addition, the matching of measured and predicted inclusion compositions allows for considerable insight into the inclusion formation processes in steel casting, including the absorption of oxygen.

The following section briefly reviews the modeling of oxygen absorption at the steel surface. Section 3 explains the method used to predict the inclusion composition in the presence of oxygen absorption. Section 4 presents the results of the predictions and the comparisons with measurements for carbon, low-alloy, and high-alloy steels. These results are discussed in Section 5. The dependence of the reoxidation rate on the free surface area and the exposure time is examined in Section 6. The conclusions of the present study are summarized in Section 7.

2   MODELING OF THE OXYGEN ABSORPTION RATE

According to the review of the literature presented in the Introduction, reoxidation of liquid steel is assumed to be controlled by the transfer of O_2 gas from the atmosphere to the atmosphere-steel interface. There, the oxygen reacts with the elements in the steel to form reoxidation inclusions. As illustrated in Fig. 2, the oxygen absorption rate can be modeled as (Sasai and Mizukami, 1996)

$$\frac{dn^O}{dt} = \frac{2\rho_a A_s}{M_a}\frac{D_a^{O_2}}{\delta_a^{O_2}}(\overline{C}_a^{O_2} - \overline{C}_{as}^{O_2}) \qquad (1)$$

where n^O is the number of moles of oxygen absorbed by the molten steel (mol), t is time (s), ρ_a

is the density of the atmosphere (g/cm^3), A_s is the surface area of the molten steel (cm^2), M_a is the molecular weight of the atmosphere (g/mol), $D_a^{O_2}$ is the mass diffusivity of O$_2$ gas in the atmosphere (cm^2/s), $\delta_a^{O_2}$ is the thickness of the concentration boundary layer of O$_2$ gas in the atmosphere (cm), $\overline{C}_a^{O_2}$ is the mole fraction of O$_2$ gas in the atmosphere far from the atmosphere-steel interface (mol/mol), and $\overline{C}_{as}^{O_2}$ is the mole fraction of O$_2$ gas in the atmosphere at the atmosphere-steel interface (mol/mol). The factor of 2 in Eq. (1) stems from the fact that one mole of absorbed O$_2$ decomposes into two moles of O in the steel. The boundary layer thickness, $\delta_a^{O_2}$, accounts for the transport properties and flow conditions of the atmosphere (see below); for example, a larger relative velocity between the steel and the atmosphere would result in a smaller boundary layer thickness and therefore, according to Eq. (1), a larger oxygen absorption rate. The ratio $D_a^{O_2}/\delta_a^{O_2}$ (cm/s) can also be interpreted as a convective mass transfer coefficient.

Equation (1) can be rewritten in terms of partial pressures, by employing the ideal gas law, as

$$\frac{dn^O}{dt} = 2A_s \frac{D_a^{O_2}}{\delta_a^{O_2}} \frac{\left(p_a^{O_2} - p_{as}^{O_2}\right)}{RT} \tag{2}$$

where $p_a^{O_2}$ is the partial pressure of O$_2$ gas in the atmosphere far from the atmosphere-steel interface (Pa), $p_{as}^{O_2}$ is the partial pressure of O$_2$ gas in the atmosphere at the atmosphere-steel interface (Pa), R is the universal gas constant [$R = 8.314 \times 10^6$ Pa cm^3/(mol K)], and T is the absolute temperature (K). The partial pressure of O$_2$ gas in the atmosphere at the atmosphere-steel interface, $p_{as}^{O_2}$, is much lower than $p_a^{O_2}$ (Sasai and Mizukami, 1996) and can safely be neglected. Then it can be seen that the oxygen absorption rate is linearly proportional to the partial pressure of O$_2$ gas in the atmosphere, as mentioned in the Introduction.

For the purpose of the present study, it is necessary to convert the number of moles of absorbed oxygen into an oxygen mass fraction (per mass of steel). For a small oxygen mass relative to the mass of steel, the mass fraction, or simply 'concentration', of absorbed oxygen, C^O (g/g), is given by

$$C^O = \frac{n^O M^O}{m_s} \tag{3}$$

where M^O is the atomic weight of oxygen (g/mol). The mass of steel, m_s, is as of now undefined. However, for the above definition of a mass fraction to be useful, it must refer to that portion of the steel where the oxygen concentration is uniform. Obviously, the oxygen does not need to be evenly distributed in the steel during pouring, and m_s could be less than the total mass of steel poured. This issue is further discussed in Section 5. After substitution of Eq. (3), Eq. (2) becomes

$$\frac{dC^O}{dt} = \frac{2A_s M^O}{m_s} \frac{D_a^{O_2}}{\delta_a^{O_2}} \frac{p_a^{O_2}}{RT} \tag{4}$$

In order to demonstrate the validity of Eq. (4), and to illustrate the effect of the boundary layer thickness, Eq. (4) is compared in the following to the experimental results of Sasai and Mizukami (1996). The experiments involved the oxidation of various iron melts that were either in a still state or stirred by an electromagnetic field. The melts were contained in crucibles and exposed at the top surface to various Ar-O_2 atmospheres at 1 atm. Both pure Fe melts and Fe-Al melts were investigated. For the Fe-Al melts, 0.1 wt% aluminum was added to the electrolytic iron. In some experiments, 0.1 wt% sulfur was added to the Fe and Fe-Al melts. For the experiments in the still state, 500 g of iron was melted in a cylindrical alumina crucible, having an inside diameter of 4 cm and a height of 15 cm. The partial pressure of O_2 gas in the Ar-O_2 atmosphere was varied over the range of 5 to 50 kPa. For the experiments in the stirred state, 70 to 80 kg of iron was melted in a cylindrical magnesia crucible, having an inside diameter of 22 cm and a height of 40 cm. Here, the partial pressure of O_2 gas was varied from 4 to 20 kPa. Other details of the experimental setup can be found in Sasai and Mizukami (1996). For the purpose of comparing the measured oxygen absorption rates to Eq. (4), the entire mass of the melt is used for m_s, implying that the oxygen is assumed to be well-mixed inside the crucibles. The mass diffusivity of O_2 in Ar at 1600°C is equal to 4.37 cm^2/s (Bird et al., 1960).

Figure 3 shows plots of the oxygen absorption rate as a function of the partial pressure of O_2 gas in the atmosphere. It can be seen from the log-log plots that the measured oxygen absorption rate (symbols) indeed varies linearly with the O_2 partial pressure, as predicted by Eq. (4). This relationship is not affected by the addition of Al or S to the iron melts, indicating that internal diffusion of Al or S does not control oxidation of the melts. The above observations are true for both the experiments in the still state (Fig. 3a) and the stirred state (Fig. 3b). In order to directly compare the predictions from Eq. (4) to the measured data, the boundary layer thickness, $\delta_a^{O_2}$, must be known. Unfortunately, it is difficult to estimate $\delta_a^{O_2}$ from the information provided in Sasai and Mizukami (1996). Therefore, $\delta_a^{O_2}$ was varied until the predictions fit the data (this corresponds to an up or down shift of the straight lines in Fig. 3). Using this method, the boundary layer thickness was found to be equal to 7.9 cm for the experiments in the still state and 0.98 cm for the stirred state. As expected, stirring the melt greatly decreases the boundary layer thickness in the atmosphere, because of the increased relative velocity between the melt and the atmosphere. This decrease in $\delta_a^{O_2}$ causes an approximately 8-fold increase in the oxygen absorption rate due to stirring. While the values obtained for $\delta_a^{O_2}$ appear realistic, more detailed comparisons are not possible. Additional discussion on the calculation of the boundary layer thickness can be found in Section 5.

3   CALCULATION OF REOXIDATION INCLUSION COMPOSITION

The composition of reoxidation inclusions as a function of steel composition and oxygen absorption rate is calculated in the present study using the software Thermo-Calc, Version P (Sundman, 2002). This thermo-chemical analysis software for multi-phase equilibrium calculations in multi-component systems requires databases for the free energy functions and

other basic data. The thermodynamic data for steel was taken from the TCAB steels/alloys database (TCFE) and that for the oxides from the SGTE substances database (SSUB). Thermo-Calc is used in the present study in conjunction with an algorithm that steps down the temperature of the system and adds oxygen at a specified rate, as explained in the following. This way, the cooling of the liquid steel and the absorption of oxygen from the atmosphere during pouring are approximated. Both full equilibrium ("lever rule") and Scheil-type analyses are performed.

For a given temperature, T, pressure, P, and mass fraction of element i in the system, C^i, Thermo-Calc calculates, among other quantities, the mass fraction of each phase k in the system, f_k, and the mass fraction of each element i in phase k, C_k^i, assuming complete thermodynamic equilibrium. This relation between the input and output parameters can be written as

$$\left(T, P, C^i\right) \rightarrow \left(f_k^*, C_k^{i*}, \cdots\right) \tag{5}$$

where the superscript * denotes an equilibrium value. Note that $C^i = \sum_k f_k^* C_k^{i*}$. The calculations are started at a temperature T_0 that corresponds to the pouring temperature of the steel (e.g., 1,600 ^{o}C). The initial values for C^i are given by the composition of the steel exiting from the ladle, and the pressure P is always kept at 1 atm. After completing the calculations at the temperature T_0 and outputting the phase fractions and compositions, the temperature is decreased by a small step, ΔT (less than 5 K), and the Thermo-Calc calculations represented by Eq. (5) are performed again at the new temperature. This procedure is repeated until room temperature (20 ^{o}C) is reached.

The absorption of oxygen is included in the Thermo-Calc calculations in the following manner. It is assumed that a certain total mass of oxygen (per mass of steel), ΔC^O, is absorbed during the time interval between the initial temperature, T_0, and the liquidus temperature, T_l, of the steel. This total amount can be obtained by integrating the oxygen absorption rate given by Eq. (4) over the time interval the steel cools from T_0 to T_l. However, in the following section, ΔC^O is simply treated as an adjustable parameter. If there are n temperature steps between T_0 and T_l, the concentration of oxygen, C^O, is then increased at each step by an amount equal to $\Delta C^O/n$. Hence, as a first approximation, it is assumed that the oxygen absorption rate is constant during pouring. The initial oxygen concentration is assumed to be negligibly small, and no oxygen is added after the liquidus temperature is reached. Below the liquidus temperature, a solid shell forms that protects the steel from further oxidation.

The above procedure constitutes the complete algorithm for the so-called "lever rule" analysis. In the lever rule approach, diffusion is assumed to be infinitely fast, such that the chemical species are well-mixed within each phase, and complete equilibrium is maintained at all times. As a consequence, previously formed phases can readily disappear at a lower

temperature where they may not be thermodynamically stable. The assumption of infinitely fast diffusion can become particularly inappropriate once the steel solidifies, because the mass diffusivities of the various elements in steel are usually several orders of magnitude lower in solid phase than in the liquid phase. Hence, as an alternative approach, a standard Scheil analysis is also performed. In the Scheil approach, diffusion in the solid phase is assumed to be negligibly small, while the liquid is still taken to be well-mixed. Therefore, previously formed solid phases cannot dissolve. The calculation procedure for the Scheil analysis is similar to that for the lever rule method, except that at the beginning of each temperature step, the concentrations, C^i, are reset to the concentrations in the liquid steel, $C_l^{i'}$, from the previous temperature step (as denoted by the prime). Also, the new phase fractions are not simply the equilibrium values, f_k^*, but must be calculated from $f_k = f_k' + f_l^* \cdot f_k^*$. These and other procedures involved in the Scheil analysis are further explained in the Thermo-Calc manual (Sundman, 2002). The results presented in the next section illustrate the differences between the lever rule and Scheil approaches, as well as their effect on the prediction of reoxidation inclusion composition.

4   RESULTS

The results of the reoxidation inclusion composition calculations are presented in this section separately for carbon steel and low- and high-alloy steels. The effects of the oxygen absorption rate, ΔC^O, and the steel composition are investigated, and the predicted inclusion compositions are compared with measured data.

4.1 CARBON STEEL

The calculations for carbon steel are intended to correspond to the measurements of reoxidation inclusion composition by Lyman and Boulger (1961). In the experiments by Lyman and Boulger, approximately 400 carbon steel plate castings were poured from 62 experimental heats. The castings ranged in size from 41 to 113 kg (90 to 250 pounds). A green sand mold was used for most of the castings. The pouring temperature was taken as 1600 °C. The nominal steel compositions are provided in Table 1. Both high-Al (0.15 wt%) and low-Al (0.05 wt%) carbon steels were investigated. The Mn content was varied from 0.4 wt% to 3.0 wt%.

4.1.1 High-Al Carbon Steel

Figure 4 shows the evolution of the oxide mass fractions (per mass of steel) as a function of temperature for the high-Al carbon steel (Table 1), calculated using the lever rule method. For the purpose of this figure, the mass fraction of absorbed oxygen, ΔC^O, is taken to be 0.9 wt%. It can be seen that the total mass fraction of all oxides increases almost linearly until the liquidus temperature, T_l, is reached (Fig. 4a). This increase is not completely linear, even though the oxygen absorption rate is assumed to be constant, because of the different molecular weights of the various oxides that form. Below the liquidus temperature the total oxide mass fraction is

approximately constant, since no more oxygen is added, except for small variations due to the continually changing composition of the oxides (Fig. 4b).

Focusing first on the temperature range above liquidus (Fig. 4a), it can be seen that the first oxide to form is solid Al_2O_3. After all of the Al is consumed, Si begins to oxidize (starting at approximately 1590 °C). At first, Si is oxidized by forming solid $Si_2O_4\_Al_6O_9$. After the solid Al_2O_3 is completely converted, solid Cristobalite (SiO_2) starts to form. At approximately the same temperature (~1585 °C), CO gas also starts to form. Finally, at approximately 1560 °C, Mn begins to oxidize by forming liquid Tephroite (Mn_2SiO_4). At the liquidus temperature, the oxide mixture consists of liquid Tephroite (Mn_2SiO_4), solid $Si_2O_4\_Al_6O_9$, solid Cristobalite (SiO_2), and CO gas; the individual mass fractions are listed in Table 3. Obviously, the CO gas will occupy a very large volume and can be expected to escape from the steel and burn up, but the present method treats the system as closed other than for the oxygen addition. The fact that more than half of the oxides (excluding CO gas) are in a liquid state agrees qualitatively with the observation made in connection with Fig. 1b regarding the globular shape of reoxidation inclusions.

Figure 4b shows the predicted evolution of the oxide mass fractions all the way down to room temperature. Between about 1500 °C and 1100 °C, the Tephroite (Mn_2SiO_4) mass fraction continues to increase, mostly at the expense of the CO gas. Note that the Tephroite is converted from liquid to solid at about 1350 °C; at 500 °C, the Tephroite is then converted to solid $Mn_2O_2\_SiO_2$. The aluminum oxide in the solid $Si_2O_4\_Al_6O_9$ is bound in the $MnO\_Al_2O_3$ phase at temperatures below 1100 °C and in Al_2FeO_4 below 1050 °C. Another iron containing oxide, liquid Fayalite (Fe_2SiO_4), forms at 900 °C; this liquid phase is then converted to solid $Fe_2O_2\_SiO_2$ at about 300 °C. The CO gas is completely consumed at a temperature slightly below 900 °C. The Cristobalite (SiO_2) also undergoes several transformations as the temperature decreases, including to Tridymite (SiO_2) and Quartz (SiO_2). The reader is referred to the figure for details on these and other intermediate transformations. At room temperature, the oxide mixture is predicted to consist of $Mn_2O_2\_SiO_2$, $Fe_2O_2\_SiO_2$, Al_2FeO_4, and SiO_2, all in the solid state. Clearly, most of the transformations shown in Fig. 4b are unlikely to occur in reality, because of the slow rate of mass diffusion in the solid and the fact that the CO gas will escape from the system and burn. The results in Fig. 4 are simply the equilibrium oxide phase fractions as a function of temperature, as predicted in a lever rule analysis.

Figure 5 shows the corresponding results using the Scheil approach. As in Fig. 4, the first phase to form is solid Al_2O_3. However, once the entire Al is consumed, the Al_2O_3 phase fraction remains constant, i.e., the alumina is not consumed in other reactions. The inability of already formed oxides to be consumed in other reactions is the main consequence of the Scheil analysis, as noted in the previous section. The ensuing sequence of Si, C, and Mn oxidation is similar to that observed in Fig. 4. At the liquidus temperature, the oxide mixture is predicted by the Scheil

analysis to consist of liquid Tephroite (Mn_2SiO_4), solid Cristobalite (SiO_2), solid Al_2O_3, and CO gas; again, the individual mass fractions are listed in Table 3. No changes in the oxide phase fractions are predicted by the Scheil analysis for temperatures below liquidus. This illustrates the limitation of the Scheil analysis, since at least some further transformation of the liquid Tephroite can be expected to occur at lower temperatures.

The differences between the lever rule and Scheil results observed in Figs. 4 and 5 must be reconciled, before the measured and predicted inclusion compositions can be compared. This is accomplished in the present study by the following conversion method. First, the mass fractions of the complex oxides (e.g., Mn_2SiO_4, $Si_2O_4\_Al_6O_9$) at the liquidus temperature are converted into equivalent mass fractions of simple oxides (e.g., SiO_2, MnO, Al_2O_3) using the chemical balances shown in Table 2. It is such simple oxides that were measured in the experiments of Lyman and Boulger (1961) and Griffin and Bates (1986a, 1986b). Then, the equivalent oxide mass fractions in the system (i.e., per mass of steel) are converted to oxide mass fractions in the inclusion, where 'inclusion' is defined as the sum of all oxides except the CO gas. The CO gas is excluded from the inclusion composition calculations, since it can be assumed to have escaped from the inclusion when the liquidus temperature is reached. The results of these conversions are shown in Table 3 for the Thermo-Calc predictions in Figs. 4 and 5. It can be seen that the equivalent inclusion oxide fractions from the lever rule and Scheil analyses are very close to each other, even though the actual oxide fractions in the system are quite different. This similarity in the inclusion composition predictions from the lever rule and Scheil analyses was observed for all steels investigated in the present study. Therefore, only results from the lever rule approach are presented in the remainder of this paper. This was done for convenience only, because the lever rule computations are very fast. In fact, the Scheil predictions can be expected to be much closer to reality, because mass diffusion in the solid state is extremely slow.

In Figs. 4 and 5, the mass fraction of absorbed oxygen, ΔC^O, was taken to be 0.9 wt%. The effect of the oxygen absorption rate on the oxide phase formation and the inclusion composition is investigated in Fig. 6. Figure 6a shows that the mass fractions (per mass of steel) of the oxides at the liquidus temperature, as predicted by the lever rule method, vary considerably with ΔC^O. For $\Delta C^O < 0.4$ wt%, no CO gas and liquid Tephroite are predicted to form. For $\Delta C^O > 1.2$ wt%, two Fe containing oxides form: solid Al_2FeO_4 and liquid Fayalite (Fe_2SiO_4). The variations in the inclusion composition with ΔC^O, calculated using the above conversion method, are plotted in Fig. 6b. It can be seen that for very low oxygen absorption rates (i.e., $\Delta C^O < 0.1$ wt%), the inclusions are predicted to consist of Al_2O_3 only. With increasing ΔC^O, first SiO_2, then MnO, and finally FeO are predicted to be present in the inclusions. At the oxygen fractions where new oxides are formed, the fractions of the previously formed oxides decrease, since the inclusion oxide fractions must always add up to 100%.

9

The results in Fig. 6b are now compared to the experimental measurements of Lyman and Boulger (1961). For the high-Al carbon steel castings with the nominal Mn content of 0.8 wt% (Table 1), the measured inclusion composition, averaged over 28 separate samples, is indicated as symbols in Fig. 6b. In this and several subsequent figures, the numbers next to the symbols denote the number of samples. The symbols were shifted along the horizontal axis until the measured and predicted Al_2O_3 and SiO_2 contents agreed. As can be seen in Fig. 6b, an excellent match for both contents occurs for a mass fraction of absorbed oxygen, ΔC^O, of 0.9 wt%. For smaller ΔC^O, the Al_2O_3 and SiO_2 contents would be over-predicted, and the reverse would be true for larger ΔC^O. The MnO content is over-predicted for $\Delta C^O = 0.9$ wt%; however, note that the sum of the measured MnO and FeO percentages agrees very well with the predicted MnO content at $\Delta C^O = 0.9$ wt%. It is reasonable to add the MnO and FeO percentages because (i) once FeO forms it does so at the expense of MnO only (see Fig. 6b), (ii) FeO could form as the liquid Tephroite (Mn_2SiO_4) is transformed during cooling to room temperature (see Fig. 4b), and (iii) MnO and FeO have very similar molecular weights. In summary, after adding the measured MnO and FeO percentages, all measured and predicted inclusion oxide percentages match for $\Delta C^O = 0.9$ wt%. This agreement provides some confidence in the present method for calculating inclusion compositions. The significance of the 0.9 wt% value for the mass fraction of absorbed oxygen, ΔC^O, obtained by matching the measured and predicted inclusion compositions, is discussed in the next section.

Figures 7 to 10 explore the effect of variations in the steel composition on oxide formation and inclusion composition. In these figures, the mass fraction of absorbed oxygen is kept constant at $\Delta C^O = 0.9$ wt%. In Fig. 7, the Mn content is varied from 0.1 wt% to 3.6 wt%. The resulting effect on the oxide mass fractions at the liquidus temperature (predicted by the lever rule method) is shown in Fig. 7a. As expected, the fraction of Mn containing oxides, in particular liquid Tephroite, increases with increasing Mn content. Interestingly, the fraction of CO gas decreases with increasing Mn content and no CO gas is formed for a Mn fraction above about 3.0 wt%. The inclusion composition is plotted as a function of the Mn content in Fig. 7b. For a Mn content in the steel of up to about 1.6 wt%, the fraction of MnO in the inclusions increases strongly with increasing Mn content, while those of SiO_2 and Al_2O_3 decrease proportionally. Beyond 1.6 wt% Mn, the inclusion composition is predicted to be approximately independent of the Mn content in the steel. Also included in Fig. 7b are the inclusion compositions measured by Lyman and Boulger (1961) for Mn contents of 0.8 wt% (nominal), 1.6 wt%, and 3.0 wt% (for the high-Al carbon steel of this subsection). As in Fig. 6b, the measured MnO and FeO contents are summed up. While the measured and predicted inclusion compositions agree very well for the nominal Mn content of 0.8 wt%, as already observed in Fig. 6b, some disagreement is present at higher Mn contents. The MnO content in the inclusion is predicted to increase more strongly with increasing Mn content in the steel than measured. On the other hand, the measured trend of the SiO_2 content in the inclusion decreasing for an increase in the Mn content from 0.8 wt% to 3.0 wt% is captured correctly by the calculations. The higher value of the measured Al_2O_3

percentage at 3.0 wt% Mn, relative to the ones at the lower Mn contents, is difficult to explain since the Al content in the steel was presumably held constant. Note that, since the oxide inclusion percentages must add up to 100, a higher percentage in one oxide will necessarily cause other percentages to be smaller. One possible explanation for the higher Al_2O_3 percentage measured at 3.0 wt% Mn may be that more of the solid Al_2O_3 particles are "captured" by the liquid Tephroite, since the Tephroite mass fraction increases with increasing Mn content (Fig. 7b). It is also possible that the oxygen absorption rate changes with the Mn content in the steel, due to changes in the CO gas formation, as shown in Fig. 7a. The CO gas (or its combustion product) may shield the metal stream from atmospheric oxygen, such that the oxygen absorption rate would increase with increasing Mn content (as less CO is formed). However, in view of Fig. 6b, only a lower rather than a higher ΔC^O would explain the measured inclusion composition at 3.0 wt% Mn. Finally, note that the measurements at the higher Mn contents represent relatively few samples, which could introduce some uncertainties.

Figure 8 shows the variations in the predicted oxide mass fractions at the liquidus temperature (Fig. 8a) and inclusion composition (Fig. 8b) with the Si content increasing from 0.1 wt% to 1.0 wt%. It can be seen from Fig. 8a that the mass fractions of CO gas and liquid Tephroite (Mn_2SiO_4) decrease with increasing Si content, and above about 0.8 wt% Si all oxides are predicted to be in the solid state at the liquidus temperature. The calculated inclusion compositions in Fig. 8b show that the increase in the SiO_2 content with increasing Si is fully at the expense of the MnO content, while the Al_2O_3 percentage is relatively constant. Above 0.8 wt% Si, MnO is completely absent from the reoxidation inclusions, such that they consist of SiO_2 and Al_2O_3 only, and the inclusion composition becomes independent of the Si content.

Figure 9a investigates the effect of the Al content on oxide formation. As expected, the fraction of aluminum oxide increases with increasing Al content. All other oxide phase fractions decrease slightly, since the total amount of oxygen absorbed is fixed. The plot of the inclusion composition in Fig. 9b indicates that the SiO_2 content is relatively unaffected by the Al content, and that the increase in the Al_2O_3 content is mostly accommodated by a decrease in the MnO percentage.

Finally, Fig. 10 illustrates the effect of the carbon (C) content. As the C content increases from 0.1 wt% the CO gas mass fraction at the liquidus temperature increases linearly, until the CO gas fraction reaches an approximately constant value at around 1.0 wt% C (Fig. 10a). Also, the liquid Tephroite mass fraction decreases steeply with increasing C content and vanishes completely at about 0.7 wt% C. No other liquid phase is present at higher C contents. The calculated inclusion composition as a function of the C content is shown in Fig. 10b. Below 0.7 wt% C, the MnO percentage decreases and the SiO_2 and Al_2O_3 percentages increase with increasing C content. Between 0.7 and 1.3 wt% C, the inclusion consists of SiO_2 and Al_2O_3 only. However, the SiO_2 content decreases in this range, and above 1.3 wt% C the inclusion consists of

11

Al$_2$O$_3$ only. Obviously, such high C contents are not used in cast steels, but the trends are nonetheless interesting.

4.1.2 Low-Al Carbon Steel

A separate set of experiments were conducted by Lyman and Boulger (1961) for low-Al carbon steel, where the Al content was only 0.05 wt% (see Table 1). The nominal Mn content was 0.4 wt%, as opposed to the 0.8 wt% for the high-Al steel of the previous subsection. Figures 11a and 11b show the predicted variation of the oxide mass fractions at the liquidus temperature and the inclusion composition, respectively, as a function of the mass fraction of absorbed oxygen, ΔC^O. This figure is analogous to Fig. 6 for the high-Al carbon steel. Figure 11b is used to determine the mass fraction of absorbed oxygen, ΔC^O, by matching the measured and predicted inclusion compositions. In this case, the data points were shifted along the horizontal axis until the measured SiO$_2$ content fell exactly on the curve representing the predicted SiO$_2$ content. Interestingly, the same $\Delta C^O = 0.9$ wt% value is obtained as for the high-Al carbon steel (Fig. 6b). With that value for the mass fraction of absorbed oxygen, the measured and predicted Al$_2$O$_3$ and MnO + FeO contents also agree very well. Note that the Al$_2$O$_3$ content in the inclusion is much lower for the present low-Al carbon steel than for the high-Al carbon steel (Fig. 6b). The match in Fig. 11b is unique in that no other ΔC^O would result in a match of all inclusion oxide fractions.

Figure 12 investigates the effect of the Mn content in the low-Al carbon steel on the oxide formation and inclusion composition, with ΔC^O kept constant at 0.9 wt%. This figure is similar to Fig. 7 for the high-Al carbon steel. The inclusion composition measurements of Lyman and Boulger (1961) are indicated as symbols in Fig. 12b and correspond to Mn contents of 0.4 wt% (nominal), 0.8 wt%, 1.6 wt%, and 3.0 wt%. Overall, the trends observed in the measured data are predicted correctly. The MnO content increases, the SiO$_2$ content decreases, and the Al$_2$O$_3$ content is approximately constant with increasing Mn content. Above 1.6 wt% Mn, the inclusion composition becomes independent of the Mn content. Some disagreement between the measured and predicted inclusion compositions exists at the higher Mn contents, as already observed for the high-Al carbon steel in connection with Fig. 7b, but no definite conclusions can be drawn with respect to the origin of the differences. Nonetheless, the comparisons provide some confidence in the present method for calculating the inclusion composition during reoxidation.

4.2 ALLOY STEEL

Griffin and Bates (1986a, 1986b) optically and chemically analyzed macro-inclusions from both low-alloy and high-alloy steel castings. The measurements of reoxidation inclusion composition used in the following are from test plates that were cast in both sand and special ceramic molds. The geometry of the test plate is shown in Fig. 13. The pouring weight of the plate was approximately 90.7 kg (200 lb), and the casting weight was about 43.1 kg (95 lb). The

pouring temperature was about 1600 °C.

From among the steels investigated by Griffin and Bates (1986a, 1986b), one low-alloy and one high-alloy steel were selected for analysis here. Their nominal compositions are provided in Table 1. The high-alloy steel corresponds to CF8M. The reoxidation inclusion compositions measured by Griffin and Bates (1986a, 1986b) for these two steels are summarized in Tables 4 and 5. For the low-alloy steel (Table 4), both matrix phase and bulk inclusion compositions are provided. They differ primarily in the Al_2O_3 content. For the matrix phase, the Al_2O_3 content is relatively constant for all 8 specimens, with the average equal to 22 wt%; this matrix phase is the actual reoxidation product. On the other hand, the bulk Al_2O_3 contents in Table 4 vary strongly and are, on the average, much higher (about 60%). The higher bulk Al_2O_3 content can be explained by the reoxidation inclusions (i.e., the matrix phase) "capturing" small Al_2O_3 deoxidation inclusion particles during filling of the mold. These deoxidation inclusions are already present in the steel in the ladle. They are captured by the rapidly moving, partially liquid reoxidation inclusions during filling (Carlson and Beckermann, 2004). The strong variations in the bulk Al_2O_3 content are due to the 8 specimens being from different test plates that were poured under different conditions and from heats with different deoxidation practices. No such distinction between matrix and bulk inclusion compositions is made for the high-alloy steel. The compositions of the 10 inclusion specimens listed in Table 5 for the CF8M steel are all relatively similar and represent reoxidation products.

4.2.1 Low-Alloy Steel

Figure 14 shows the effect of the mass fraction of absorbed oxygen, ΔC^O, on oxide formation and inclusion composition for the low-alloy steel. This figure is similar to Figs. 6 and 11 for the carbon steels, and the reader is referred to the previous subsections for a more detailed discussion. The main difference from these earlier figures is that for the low-alloy steel a Cr containing oxide forms for ΔC^O greater than about 1.1 wt% (Fig. 14a). In the same manner as in the previous subsections, Fig. 14b is used to determine the mass fraction of absorbed oxygen, ΔC^O, by matching the measured and predicted inclusion compositions. According to the above discussion, the average matrix phase composition in Table 4 represents the measured reoxidation inclusion composition. Note that no FeO was detected in the inclusions (Table 4); hence, the measured MnO and FeO do not need to added up as was done for the carbon steels. The measured CaO content (3 wt%) is simply neglected. Figure 14b shows that $\Delta C^O = 0.9$ wt% provides a good match between the measured and predicted inclusion compositions. The matching was performed based on the SiO_2 and MnO contents only. The measured Al_2O_3 content of 22 wt% was primarily used to determine the Al content in the steel, because the Al content was not provided by Griffin and Bates (1986b). The resulting value of 0.2 wt% Al (see Table 1) is realistic and, together with $\Delta C^O = 0.9$ wt%, provides for excellent agreement between the measured and predicted inclusion compositions. Interestingly, the 0.9 wt% value for the mass fraction of absorbed oxygen is the same as was determined for the carbon steels.

13

With an Al_2O_3 content of 22% in the matrix phase created by reoxidation, the measured Al_2O_3 bulk inclusion percentages can be used to back out the mass fraction of deoxidation inclusions for each of the specimens in Table 4. The result is shown in Fig. 15. It can be seen that between 0.5 wt% and 4 wt% Al_2O_3 deoxidation inclusions must be present in the steel to explain the high values of the measured Al_2O_3 bulk inclusion percentages. For example, a measured Al_2O_3 content of 60 wt% in the bulk inclusion corresponds to 2 wt% Al_2O_3 in the steel before any oxygen is added. Such high deoxidation inclusion mass fractions are not realistic. The high values simply reflect the fact that the solid Al_2O_3 deoxidation inclusions are not uniformly distributed in the liquid steel, but are captured by the reoxidation inclusions during filling, as discussed above. Nonetheless, it is useful to see from Fig. 15 that the measured variations in the SiO_2 and MnO bulk inclusion percentages can be explained by the presence of Al_2O_3 deoxidation inclusions.

4.2.2 High-Alloy Steel (CF8M)

Figure 16 shows the predicted variation of the oxide mass fractions in the high-alloy steel (CF8M; see Table 1) with temperature, for the lever rule approach and a mass fraction of absorbed oxygen of 0.9 wt%. The nominal Si content of 1.33 wt% in Table 1 was not specified by Griffin and Bates (1986a). The method used to determine both the Si content and the mass fraction of absorbed oxygen is explained below in connection with Fig. 17. It can be seen from Fig. 16a that solid Cristobalite (SiO_2) is the first oxide to form as the temperature decreases from 1600 ^{o}C. At about 1500 ^{o}C, all of the Si is oxidized, and solid Cr_2O_3 starts to form. At the liquidus temperature, the Cristobalite is transformed into Tridymite (SiO_2) and the Cr_2O_3 mass fraction reaches a maximum. No liquid or gaseous oxides (e.g., CO) are present at the liquidus temperature. Below the liquidus temperature (Fig. 16b), the SiO_2 mass fraction increases at the expense of Cr_2O_3, and at slightly below 900 ^{o}C all of the Cr_2O_3 is decomposed. Also, the Tridymite (SiO_2) is transformed into Quartz (SiO_2). At about 700 ^{o}C, Mn is starting to oxidize by forming solid Tephroite (Mn_2SiO_4). Finally, at about 300 ^{o}C, some of the Quartz (SiO_2) and all of the Tephroite (Mn_2SiO_4) are consumed to form solid $Mn_2O_2\_SiO_2$. Again, the numerous solid state transformations predicted by the lever rule method as room temperature is approached are unlikely to be completed due to the slow rate of mass diffusion in the solid. Although no Mn oxides are present at the liquidus temperature, Fig. 16 shows that it is thermodynamically possible for Mn oxides to be present at room temperature.

Figure 17 shows the calculated variation of the inclusion composition with Si content (Fig. 17a) and ΔC^O (Fig. 17b). These inclusion compositions were obtained using the same conversion method as explained above in connection with the carbon steels. It can be seen from Fig. 17a that below about 0.65 wt% Si, the inclusions are predicted to consist entirely of Cr_2O_3. For larger Si contents, the SiO_2 percentage in the inclusions increases at the expense of Cr_2O_3. For Si contents above about 1.6 wt%, the inclusions consist entirely of SiO_2. Figure 17b shows

that for ΔC^O below 0.6 wt%, the inclusions are also predicted to be 100% SiO$_2$. For larger ΔC^O, the Cr$_2$O$_3$ content increases at the expense of SiO$_2$.

The mass fraction of absorbed oxygen, ΔC^O, and the Si content in the CF8M steel are both determined by matching the measured and predicted inclusion compositions. The average values in Table 5 are used as the measured composition, neglecting the small percentages of FeO, TiO$_2$, and Al$_2$O$_3$. Table 5 shows that the inclusions analyzed by Griffin and Bates (1986a) contained, on the average, about 11 wt% MnO. Unfortunately, as shown in Fig. 17, no MnO is predicted to be present in the inclusions using the present conversion method. However, as explained in connection with Fig. 16, it is possible for Mn oxides to form in the solid state as room temperature is approached. The lever rule predictions in Fig. 16 also show that it is possible for the Cr$_2$O$_3$ to be decomposed at lower temperatures. These solid state transformations are not modeled in the present study. Nonetheless, based on this discussion, it appears to be reasonable to add up the measured MnO and Cr$_2$O$_3$ percentages and compare them to the predicted Cr$_2$O$_3$ percentage. A series of calculations were performed where both ΔC^O and the Si content were varied (not shown here), until the predicted SiO$_2$ and Cr$_2$O$_3$ percentages matched with the measured SiO$_2$ and MnO + Cr$_2$O$_3$ percentages. A unique match was obtained for $\Delta C^O = 0.9$ wt% and a Si content of 1.33 wt%, as shown in Fig. 17. This Si content is reasonable for CF8M steel. Interestingly, the obtained value of 0.9 wt% for the mass fraction of absorbed oxygen is the same as for the carbon and low-alloy steels (see above).

For completeness, the effects of variations in the Mn and Cr content on the inclusion composition for the CF8M steel are shown in Figs. 18a and 18b, respectively. Within the range of 0.5 wt% to 1.5 wt% plotted in Fig. 18a, the Mn content does not have a strong influence on the inclusion composition. On the other hand, increasing the Cr content from 18 wt% to 21 wt% causes a significant increase in the Cr$_2$O$_3$ content in the inclusions from about 30% to 55%, with the SiO$_2$ content decreasing proportionally (Fig. 18b).

5 DISCUSSION

The results in the previous section show that the composition of reoxidation inclusions in casting of carbon and low-/high-alloy steels can be successfully predicted using the present approach. The inclusion composition was found to be very sensitive to the amount of oxygen absorbed by the steel. Interestingly, for all experiments analyzed in the present study, the matching of measured and predicted inclusion compositions resulted in the same value (i.e., 0.9 wt%) for the mass fraction of absorbed oxygen per mass of steel, ΔC^O. Thus, the main questions remaining are why ΔC^O is the same for all cases analyzed here and how the value of 0.9 wt% can be achieved. The oxygen absorption can generally be expected to depend on the pouring conditions (e.g., size and position of ladle), the casting system design (e.g., height of sprue, design of gates and runners), and numerous other factors. While the casting trials of Lyman and Boulger (1961) and Griffin and Bates (1986a, 1986b) were not exactly the same, all of them

involved plates of similar size that were cast using a relatively "standard" filling system (i.e., steel is poured from a ladle into a vertical sprue with a fall height of about 1 m). This similarity may explain why ΔC^O was the same for these casting trials. If the plates had been cast using a vacuum-assisted counter-gravity pouring system, for example, ΔC^O could be expected to be much lower and the inclusion composition would have been much different.

In order to better understand how a value of 0.9 wt% for ΔC^O can be achieved, the following order-of-magnitude estimate of ΔC^O can be made based on Eq. (4). Assume, as an extreme case, that the steel being poured from the ladle into the mold consists of a stream of small spherical droplets of average radius r. Such a situation could arise if the stream is highly fragmented by a poor nozzle design (for a bottom-pour ladle) or by excessive splashing. As illustrated in Fig. 19a, each droplet can be thought of as being exposed to air flowing over it with a certain relative velocity u_a. For spherical droplets, the ratio of the surface area to the mass is given by

$$\frac{A_s}{m_s} = \frac{3}{\rho_s r} \tag{6}$$

where ρ_s is the steel density taken as 7.8 g/cm³. Substituting Eq. (6) into Eq. (4) and integrating Eq. (4) over the time the droplet is exposed to air, t_e, yields the following expression for the mass fraction of absorbed oxygen

$$\Delta C^O = \frac{6M^O}{\rho_s r} \frac{D_a^{O_2}}{\delta_a^{O_2}} \frac{p_a^{O_2}}{RT} t_e \tag{7}$$

During integration, all variables on the right hand side of Eq. (4) were assumed constant. The molecular diffusivity of O_2 in air, $D_a^{O_2}$, at 1600 °C is equal to 4.56 cm²/s (Bird et al. 1960) and the partial pressure of O_2 in air, $p_a^{O_2}$ is equal to 21.23 kPa. Equation (7) shows that the mass fraction of oxygen absorbed by the steel droplet is proportional to the O_2 partial pressure and the exposure time and inversely proportional to the droplet radius and the boundary layer thickness.

The O_2 gas concentration boundary layer thickness, $\delta_a^{O_2}$, is a function of the relative velocity between the droplet and the air, u_a, the droplet radius and various air properties. It can be estimated from the Ranz-Marshall correlation (Ranz and Marshall, 1952) for convective mass transfer, i.e.,

$$Sh = 2 + 0.6 \, Re^{1/2} \, Sc^{1/3} \tag{8}$$

where Sh is the Sherwood number ($Sh = 2r/\delta_a^{O_2}$), Re is the Reynolds number ($Re = 2r\rho_a u_a / \mu_a$), and Sc is the Schmidt number ($Sc = \mu_a /(\rho_a D_a^{O_2})$). The density, ρ_a, and the dynamic viscosity, μ_a, of air at 1600 °C are approximately equal to 0.19×10⁻³ g/cm³ and 5.96×10⁻⁴ g/(cm·s), respectively (Kreith and Goswami, 2004). The variation of the boundary layer thickness calculated from Eq. (8) as a function of the droplet radius and the relative velocity between the droplet and the air is plotted in Fig. 19b. For $u_a = 0$, $\delta_a^{O_2}$ is simply equal to

r. For sufficiently large Reynolds numbers, the boundary layer thickness increases with droplet radius according to $\delta_a^{O_2} \sim r^{1/2}$, and decreases with increasing relative velocity according to $\delta_a^{O_2} \sim u_a^{-1/2}$. As a specific example, for a droplet radius of 1 cm and a relative velocity of 4.5 m/s, the boundary layer thickness is equal to about 0.15 cm.

Applying the above equations to the previous example of a stream of droplets, the following conservative estimates can now be made. For a typical fall height of the liquid steel from the ladle into the mold of about $h = 1$ m, an estimate of the relative velocity between the droplets and the air is then given by $u_a = \sqrt{2gh} \approx 4.5$ m/s, where $g = 9.81$ m/s^2. Considering this velocity and the distances involved, an upper limit on the exposure time can be taken as $t_e = 1$ s. The entire fill time of a mold, which is typically much longer than 1 s, cannot be taken as the exposure time, because the steel cannot be assumed to consist of droplets once it is deeper inside the mold. With these values for u_a and t_e, Eqs. (7) and (8) can be solved simultaneously for the boundary layer thickness and the droplet radius that are needed to achieve a mass fraction of absorbed oxygen, ΔC^O, of 0.9 wt%. The result is $\delta_a^{O_2} = 0.07$ cm and $r = 0.1$ cm. In other words, the liquid metal stream from the ladle into the mold would need to consist of 2 mm diameter droplets to absorb sufficient oxygen in 1 s that the observed reoxidation inclusion compositions are attained. Note that in this extreme example all of the steel (i.e., the entire droplet) is assumed to achieve $\Delta C^O = 0.9$ wt% of absorbed oxygen.

If the steel during pouring flows in a more compact manner, such as in a cylindrical jet rather than a stream of small droplets, the absorbed oxygen is not likely to be uniformly distributed in the liquid steel. Instead, the oxidation would be limited to a relatively thin layer of liquid steel adjacent to the free surface, as illustrated in Fig. 20a. In this alternative scenario, the 0.9 wt% value for the mass fraction of oxygen is only achieved in the thin oxidation layer, the reoxidation inclusions only form in this layer and the liquid steel outside of the layer is unaffected. Then, the mass of steel, m_s, in Eq. (4) is not equal to the total mass of steel poured, but only equal to the mass of the steel in the oxidation layer. An effective thickness of the oxidation layer, d_s^{ox}, may be estimated as follows. Assuming the oxidation layer to be approximately flat, the ratio of the surface area to the mass of the steel in the oxidation layer is given by

$$\frac{A_s}{m_s} = \frac{1}{\rho_s d_s^{ox}} \tag{9}$$

Substituting Eq. (9) into Eq. (4) and performing the same kind of integration as was done with Eq. (7), yields the following expression for the thickness of the oxidation layer

$$d_s^{ox} = \frac{2M^O}{\rho_s \Delta C^O} \frac{D_a^{O_2}}{\delta_a^{O_2}} \frac{p_a^{O_2}}{RT} t_e \tag{10}$$

The oxidation layer thickness calculated from Eq. (10) as a function of the exposure time, t_e, is plotted in Fig. 20b for $\Delta C^O = 0.9$ wt% and the boundary layer thickness, $\delta_a^{O_2}$, ranging from 0.1

cm to 0.5 cm. It can be seen that, as expected, the thickness d_s^{ox} of the layer where a mass fraction of 0.9 wt% of oxygen is achieved increases linearly with the exposure time. Also, d_s^{ox} increases with decreasing $\delta_a^{O_2}$ (or increasing oxygen transfer rate through the air). The correlation for the boundary layer thickness around a sphere, Eq. (8), is approximately valid for other flow geometries, including a cylindrical stream. For example, for a stream of 2.5 cm radius and a relative velocity of 4.5 m/s, $\delta_a^{O_2}$ may be estimated from Fig. 19b to be about 0.3 cm. Then, Fig. 20b shows that the oxidation layer reaches a thickness of 0.1 mm after 1 s of exposure time. Hence, a large portion of the 2.5 cm radius stream is unaffected by oxygen absorption. If the exposure time is 10 s, the oxidation layer thickness will reach 0.1 cm.

The previous two order-of-magnitude estimates represent only limiting cases for achieving the 0.9 wt% of absorbed oxygen that results in the measured and predicted reoxidation inclusion compositions to agree. They show that depending on the flow conditions, the oxygen and, hence, the inclusions may be distributed non-uniformly in the liquid steel. Therefore, in order to truly predict the inclusion composition, the complex internal transport of chemical species in the liquid steel together with the formation of the inclusions would have to be modeled in detail. The above discussion shows that such a model would need to resolve the transport processes on a microscopic scale (i.e., microns). This would be difficult to accomplish on the scale of an entire casting.

6   CALCULATION OF REOXIDATION RATES

The present model for the oxygen absorption rate (Section 2), together with the knowledge of the reoxidation inclusion composition (Sections 3 and 4), allows for the calculation of the rates at which the alloying elements in the steel (and the oxygen) are consumed, and at which the inclusions are formed. Assuming a constant boundary layer thickness, equal to some average value, and constant properties, and neglecting $p_{as}^{O_2}$ as before, Eq. (2) can be integrated over time to yield the following expression for the number of moles of absorbed oxygen

$$n^O = 2\frac{D_a^{O_2}}{\delta_a^{O_2}}\frac{p_a^{O_2}}{RT}\left(\overline{A}_s t_e\right) \tag{11}$$

where the product of the average free surface area of the liquid steel and the exposure time, $\left(\overline{A}_s t_e\right)$, is given by

$$\overline{A}_s t_e = \int A_s(t)dt \tag{12}$$

This area integral could, in principle, be obtained from the results of computer simulations of the filling process of a casting, such as those performed by virtually all commercially available casting simulation software. The integration limits would then correspond to the entire fill time of a casting. Care should be taken to include the metal stream between the ladle and the mold,

since considerable reoxidation of the steel can already occur in this generally unprotected portion of the flow. It should, however, be noted that the lack of numerical resolution in current filling simulations could cause a severe underestimation of the free surface area, especially if the flow is highly fragmented and turbulent.

The only other factor in Eq. (11) that is generally unknown is the boundary layer thickness of the oxygen in the air, $\delta_a^{O_2}$. To a good approximation, $\delta_a^{O_2}$ can be calculated from the mass transfer correlation given by Eq. (8), as a function of the free surface geometry (e.g., the radius, r, of the stream or of a droplet) and the relative velocity between the steel and the air, u_a, as shown in Fig. 19b. The boundary layer thickness can be expected to vary considerably with location in the flow and time during filling. Hence, the results of a filling simulation could be used to evaluate $\delta_a^{O_2}$ instantaneously at all points on the free surface. In that case, $\delta_a^{O_2}$ should be included in the integration represented by Eq. (12). By performing these calculations as part of a filling simulation, the effects of the pouring and gating system design on the oxygen absorption (and, hence, inclusion formation) could be investigated numerically (Carlson and Beckermann, 2004).

For the purpose of the present calculations, a representative average value for $\delta_a^{O_2}$ is estimated from Fig. 19b as follows. A lower bound on the liquid steel velocity may be taken as 1 m/s (corresponding to a fall height of only 5 cm); the velocity in typical steel casting operations will generally not exceed 10 m/s. Furthermore, due to surface tension, the free surface structures are typically not smaller than about 0.1 cm in the radius of curvature. Due to continual breakup of the streams, an upper bound on the radius in steel casting may be around 2.5 cm (1 in). Note that for these ranges of velocities and radii, the boundary layer thickness is not a strong function of the radius. In view of Fig. 19b, a representative average value for $\delta_a^{O_2}$ can then be taken as 0.15 cm (corresponding, for example, to $r = 1$ cm and $u_a = 5$ m/s).

Since all of the absorbed oxygen is consumed in the formation of inclusions, the knowledge of the number of moles of oxygen absorbed, n^O, from Eq. (11) allows for the calculation of the mass of the individual oxides formed. This calculation is straightforward, since the composition of the inclusions and the molecular weights of the oxides are known. Also, the mass of the alloying elements in the steel that are consumed in the oxidation reactions can be readily calculated. Furthermore, the volumes of the CO gas formed and of the air needed to supply the oxygen can be calculated from the ideal gas law; the pressure and temperature are simply taken as 1 atm and 25 ^{o}C, respectively.

The results of such calculations for the low-alloy steel (see Table 1) and $\delta_a^{O_2} = 0.15$ cm are shown in Fig. 21. Figure 21 shows that, as expected, the mass of the alloy elements consumed (Fig. 21a) and of the inclusions formed (Fig. 21b) increases linearly with the integrated product of the free surface area and the exposure time, $\left(\overline{A}_s t_e\right)$. Note from Eq. (11) that the total mass of

the steel poured does not enter directly into these calculations. In other words, the same value of $\left(\overline{A}_s t_e\right)$ can be achieved for different amounts of steel poured, depending on how fragmented or compact the stream is and how long the free surface is exposed to air. For example, for $\left(\overline{A}_s t_e\right) = 100$ m^{2}s (and $\delta_a^{O_2} = 0.15$ cm), 2.5 kg of solid inclusions are formed (Fig. 21b). This value of $\left(\overline{A}_s t_e\right)$ could be achieved for 1 ton of steel if the flow is highly fragmented and/or the mold filling time is very long, or for 10 tons of steel if the flow is more compact and rapid or the stream is protected. Figure 21 also shows that for every 1 kg of solid reoxidation inclusions formed (corresponding to $\left(\overline{A}_s t_e\right) \approx 40$ m^{2}s in Fig. 21), 0.2 m^3 of CO gas is produced and almost 2 m^3 of air is needed to supply the oxygen (at 25 °C and 1 atm).

Figure 21 also allows for the integrated free surface area, $\left(\overline{A}_s t_e\right)$ to be determined from the knowledge of the mass of the alloy elements consumed. A loss of about 0.73 kg Mn, 0.41 kg Si, 0.41 kg Al, and 0.14 kg C per ton of steel has been reported by Brower et al. (1950) for unprotected tapping and ladle filling operations in wrought steel production. These values are indicated in Fig. 21a as symbols. The symbols were shifted along the horizontal axis until the Mn loss (0.73 kg) agreed with the calculated value. This fit occurs for $\left(\overline{A}_s t_e\right) = 110$ m^{2}s. Although the steels investigated by Brower et al. (1950) had a somewhat different composition than the low-alloy steel to which Fig. 21 corresponds, reasonable agreement is achieved for the other consumed elements as well. There is an additional uncertainty of at least a factor of two in this value for $\left(\overline{A}_s t_e\right)$, because the boundary layer thickness, $\delta_a^{O_2} = 0.15$ cm, for which Fig. 21 was plotted represents only a rough estimate (see above). Considering typical values for the fall height and the velocity of the stream during pouring, the exposure time may be estimated as 1 s (note that the exposure time is not directly related to the mass of the steel). With $t_e = 1$ s, the average free surface area that corresponds to the measured alloy element losses would then be equal to 110 m^2. Such a high value for the free surface area indicates the presence of considerable stream roughness, splashing, and air entrainment during pouring. A free surface area of 110 m^2 for 1 ton of steel can be achieved, for example, by visualizing the metal stream during pouring to consist of droplets with a radius of about 0.35 cm. This value is not too different from the droplet size that was estimated in the previous section from the knowledge of the oxygen content necessary to predict the measured inclusion composition.

Figure 21b shows that, in the present example of unprotected tapping and ladle filling (i.e., for $\left(\overline{A}_s t_e\right) = 110$ m^{2}s), approximately 2.75 kg of solid inclusions and 0.55 m^3 of CO gas are produced. Also, 5.5 m^3 of air at standard conditions are needed to supply the oxygen. Since 1 ton of steel has a volume of only 0.13 m^3, this corresponds to an air-to-steel volume ratio of about 42. It can be expected that the above values are not much different during unprotected pouring of steel from a ladle into a mold in typical steel casting operations.

For completeness, several important reoxidation inclusion properties (average density and average molecular weight) and ratios (inclusion mass or moles per mass or moles of oxygen

consumed) are summarized in Table 6. Values are included for both low- and high-alloy steels. The table also shows the large effect of the CO gas on the inclusion density for low-alloy steel.

7   CONCLUSIONS

The model developed in this study successfully predicts the composition of reoxidation inclusions in steel castings that form due to liquid steel being exposed to air during pouring from the ladle into the mold. It is shown how the inclusion composition varies with the composition of the steel (e.g., Mn or C content) and the mass fraction of absorbed oxygen (ΔC^O). For a mass fraction of 0.9 wt% oxygen, the predicted and previously measured inclusion compositions were found to agree, regardless of the steel grade. The present model for the oxygen absorption rate shows under what conditions such high oxygen contents can be achieved. One possibility is that the liquid metal stream during pouring is highly fragmented, consisting of droplets of a few millimeters in diameter exposed to air for at least 1 second. This scenario is also supported by the fact that for unprotected liquid steel transfer operations, such as tapping and ladle filling, a similar droplet size can be estimated based on the knowledge of the mass of the consumed alloy elements in the steel. If the liquid metal stream during pouring is more compact, on the other hand, the oxygen content of 0.9 wt% can only be achieved in a relatively thin oxidation layer adjacent to the free surface. These findings point to the need for a more sophisticated reoxidation inclusion formation model. Such a model would need to account for the transport and reactions of the various chemical species inside the steel. In addition, it would need to accurately predict the free surface area during pouring and the rates of oxygen transport through the air as a function of the flow conditions.

REFERENCES

Bird, R. B., Stewart, W. E., and Lightfoot, E. N., Transport Phenomena, John Wiley & Sons, Inc., New York, 1960, pp. 512.

Brabie, V., Kawakami, M., and Eketorp, S., "The Mechanism of Formation of Oxide Macro-Inclusions Studied by Blowing Pure Oxygen into Molten Steel," Scandinavian Journal of Metallurgy, Vol. 4, 1975, pp.273-283.

Brabie, V., "Study on the Reoxidation of Liquid Steel during Teeming and its Contribution to Inclusion Formation in Liquid Steel," <u>Scandinavian Journal of Metallurgy</u>, Vol. 5, 1976, pp.185-192.

Brower, T. E., Bain, J. W., and Larsen, B. M., "Oxygen in Liquid Open Hearth Steel - Oxidation During Tapping and Ladle Filling," <u>Transactions AIME</u>, Vol. 188, 1950, pp. 851-861.

Carlson, K. D., and Beckermann, C., "Modeling of Reoxidation Inclusion Formation During Filling of Steel Castings," in <u>Proceedings of the 58th Technical and Operating Conference</u>, SFSA, Chicago, 2004.

Eijk, C., Grong, Ø., and Walmsley, J., "Mechanisms of Inclusion Formation in Low Alloy Steels Deoxidised with Titanium," <u>Materials Science and Technology</u>, Vol. 16, 2000, pp. 55-64.

Goto, H., and Miyazawa, K., "Reoxidation Behavior of Molten Steel in Non-killed and Al-killed Steels," <u>ISIJ International</u>, Vol. 38, No. 3, 1998, pp. 256-259.

Griffin, J. A., and Bates, C. E., "Development of Casting Technology to Allow Direct Use of Steel Castings in High Speed Machining Lines, Part II – Identification of Nonmetallic Inclusions in High Alloy steel Castings," SFSA Research Report SoRI-EAS-86-682, 1986a.

Griffin, J. A., and Bates, C. E., "Development of Casting Technology to Allow Direct Use of Steel Castings in High Speed Machining Lines, Part III – Identification of Oxide Macro-Inclusions in Carbon and Low Alloy Steel Castings," SFSA Research Report SoRI-EAS-86-810, 1986b.

Griffin, J. A., and Bates, C. E., "Ladle Treatment, Pouring and Gating for the Production of Clean Steel Castings," SFSA Research Report, No. 104, January 1991.

Heaslip, L. J., McLean, A. and Sommerville, I. D., "Chemical and Physical Interactions during Transfer Operations," Continuous Casting Series, <u>I.S.S. – A.I.M.E.</u>, Vol. 1, 1983, pp. 1-14.

Hsieh, K. C., Babu, S. S., Vitek, J. M., David, S. A., "Calculation of Inclusion Formation in Low-Alloy-Steel Welds," <u>Materials Science & Engineering A</u>, Vol. 215, 1996, pp. 84-91.

Kreith, F., and Goswami, D. Y., "The CRC Handbook of Mechanical Engineering," 2nd ed., CRC Press LLC, p. A-2, 2004

Lange, K. W., and Massard, P., "Oxygen Pick-up of Iron Jets by Oxidation," <u>Archiv fur das Eisenhuettenwesen,</u> Vol. 48, No. 8, 1977, pp. 415-420.

Lyman, W. S., and Boulger, F. W., "An Investigation of Factors Producing the Ceroxide Defect in Steel Castings, Part I – Composition and Sources," SFSA Research Report No. 48, February 1961.

Ranz, W. E. and Marshall, W. R., "Evaporation from drops – Part I," Chem. Eng. Prog., Vol. 48, 1952, pp. 141.

Sasai, K., and Mizukami, Y., "Effect of Stirring on Oxidation Rate of Molten Steel," ISIJ International, Vol. 36, No. 4, 1996, pp. 388-394.

Sasai, K., and Mizukami, Y., "Effects of Tundish Cover Powder and Teeming Stream on Oxidation Rate of Molten Steel in Tundish," ISIJ International, Vol. 38, No. 4, 1998, pp. 332-338.

Sasai, K., and Mizukami, Y., "Reoxidation Behavior of Molten Steel in Tundish," ISIJ International, Vol. 40, No. 4, 2000, pp. 40-47.

Sommerville, I. D., and McKeogh, E. J., "Reoxidation of Steel by Air Entrained during Casting," Continuous Casting of Steel: Proceedings of the 2nd Process Technology Conference, Chicago Meeting, Iron and Steel Society of AIME, 1981, pp. 256-268.

Sun, H., and Pehlke, R. D., "Kinetic of Oxidation of Carbon in Liquid Iron-Carbon-Silicon-Manganese-Sulfur Alloys by Carbon Dioxide in Nitrogen," Metallurgical and Materials Transactions, Vol. 26B, 1995, pp. 335-344.

Sun, H., and Pehlke, R. D., "Modeling and Experimental Study of Gaseous Oxidation of Liquid Iron Alloys," Metallurgical and Materials Transactions, Vol. 27B, 1996, pp. 854-864.

Sundman, B., Thermo-Calc User's Guide, Version P, Royal Institute of Technology, Stockholm, Sweden, 2002.

Svoboda, J. M., Monroe, R. W., Bates, C. E., and Griffin, J., "Appearance and Composition of Oxide Macroinclusions in Steel Castings," AFS Transactions, Vol. 95, 1987, pp. 187-202.

Vishkarev, A. F., and Gorokhov, L. S., "Relationships Governing Reoxidation of Steel," Steel in the USSR, Vol. 21, 1991, pp. 196-198.

LIST OF TABLES

LIST OF FIGURES

Figure 11 Effect of the mass fraction of absorbed oxygen on the oxide mass fractions at the liquidus temperature and on the inclusion composition for low-Al carbon steel. (a) Mass fraction of oxide phases at the liquidus temperature (1528 °C, lever rule). (b) Inclusion composition.

Figure 12 Effect of the Mn content on the oxide mass fractions at the liquidus temperature and on the inclusion composition for low-Al carbon steel (ΔC^O = 0.9 wt%). (a) Mass fraction of oxide phases at the liquidus temperature (1528 °C, lever rule). (b) Inclusion composition.

Figure 13 Geometry of the low- and high-alloy steel test plate castings (after Griffin and Bates, 1986a and 1986b); the unit for all lengths is inches.

Figure 14 Effect of the mass fraction of absorbed oxygen on the oxide mass fractions at the liquidus temperature and on the inclusion composition for low-alloy steel. (a) Mass fraction of oxide phases at the liquidus temperature (1528 °C, lever rule). (b) Inclusion composition.

Figure 15 Effect of the mass fraction of Al_2O_3 deoxidation inclusions on the bulk composition of the reoxidation inclusions in low-alloy steel.

Figure 16 Evolution of the mass fraction of the various oxide phases in high-alloy CF8M steel calculated using the lever rule method (ΔC^O = 0.9 wt%). (a) Temperature range: 1600 to 1300 °C. (b) Temperature range: 1600 to 20 °C.

Figure 17 Effect of the Si content and the mass fraction of absorbed oxygen on the inclusion composition for high-alloy CF8M steel. (a) Effect of Si content for ΔC^O = 0.9 wt%. (b) Effect of mass fraction of absorbed oxygen for a Si content of 1.33 wt%.

Figure 18 Effect of the Mn and Cr contents on the inclusion composition for high-alloy CF8M steel (ΔC^O = 0.9 wt%). (a) Effect of Mn content. (b) Effect of Cr content.

Figure 19 Oxygen transfer from air to a droplet of steel. (a) Schematic illustration of air flowing past a steel droplet. (b) Boundary layer thickness of O_2 gas in air as a function of droplet radius and relative velocity.

Figure 20 Oxidation layer adjacent to the free surface of the steel in which the mass fraction of absorbed oxygen reaches 0.9 wt%. (a) Schematic illustration of the oxidation layer. (b) Oxidation layer thickness as a function of exposure time and O_2 gas boundary layer thickness.

Figure 21 Mass of consumed alloying elements, volume of air need to supply the oxygen, mass of inclusions formed, and volume of CO gas formed as a function of the integrated free surface area and exposure time product for low-alloy steel ($\delta_a^{O_2}$ = 0.15 cm). (a) Mass of consumed alloying elements and volume of air. (b) Mass of inclusions and volume of CO gas formed.

Table 1 Composition of the steels investigated in the present study (wt%).

	C	Si	Mn	S	P	Al	Cr	Ni	Mo
high-Al carbon steel	0.3	0.35	0.8	0.015	0.015	0.15	-	-	-
low-Al carbon steel	0.3	0.35	0.4	0.015	0.015	0.05	-	-	-
low-alloy steel	0.26	0.39	0.83	0.017	0.019	0.2	0.45	0.52	0.16
high-alloy steel, CF8M	0.05	1.33	1.0	0.03	0.03	-	19.5	10.5	2.5

Table 2 Chemical equations used to convert between predicted and equivalent oxide fractions.

$$Si_2O_4\_Al_6O_9 = 2SiO_2 + 3Al_2O_3$$
$$Mn_2SiO_4 = SiO_2 + 2MnO$$
$$Fe_2SiO_4 = SiO_2 + 2FeO$$
$$Al_2SiO_4 = SiO_2 + Al_2O_3$$
$$MnO\_Al_2O_3 = MnO + Al_2O_3$$
$$Cr_2FeO_4 = FeO + Cr_2O_3$$
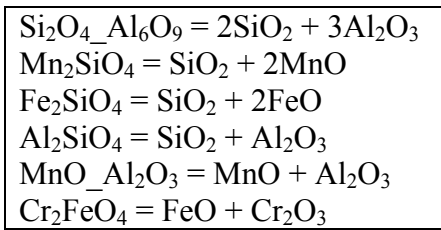
Table 3 Predicted and equivalent oxide phase fractions at the liquidus temperature for high-Al carbon steel.

$\Delta C^O = 0.9$ wt%		lever rule approach	Scheil approach
predicted oxide phase fractions per mass of steel (wt%)	CO (g)	0.429	0.331
	Al$_2$O$_3$ (s)	0	0.254
	Cristobalite (s) (SiO$_2$)	0.325	0.322
	Si$_2$O$_4$_Al$_6$O$_9$ (s)	0.395	0
	Tephroite (l) (Mn$_2$SiO$_4$)	0.934	0.738
equivalent oxide phase fractions in inclusions, excluding CO gas (wt%)	Al$_2$O$_3$	17.2	19.4
	SiO$_2$	43.1	41.2
	MnO	39.7	39.4

Table 4   Measured matrix phase and bulk inclusion compositions for low-alloy steel (wt%) (from Griffin and Bates, 1986b).

Specimen Number	Matrix Phase				Bulk Inclusion			
	Al_2O_3	SiO_2	MnO	CaO	Al_2O_3	SiO_2	MnO	CaO
103-4	24	45	20	6	42	36	15	4
106-116-2	26	42	28	5	74	15	9	2
107-103-3	18	46	36	0	61	22	16	0
109-119-4	22	43	28	5	64	26	10	1
110-107-2	19	49	28	0	75	16	8	0
110-135	19	48	29	2	61	22	16	1
111-24	20	55	20	3	65	26	7	1
112-5	25	42	34	0	40	35	25	0
Average	22	46	28	3	60	25	13	1

Table 5   Measured inclusion compositions for high-alloy steel, CF8M (wt%) (from Griffin and Bates, 1986a).

Specimen Number	SiO_2	Cr_2O_3	MnO	FeO	TiO_2	Al_2O_3
113-25	53	31	16	0	0	1
113-26	59	24	14	0	4	0
113-28	60	18	18	0	0	2
114-4	59	30	11	0	0	0
114-5	55	38	5	2	0	0
114-6	62	28	7	3	0	0
114-8	60	27	10	2	0	2
114-109-1	66	23	11	0	0	0
114-110-2	63	27	10	0	0	0
114-138-2	71	17	9	2	0	0
Average	60.8	26.3	11.1	0.9	0.4	0.5

Table 6   Predicted inclusion properties and ratios for low- and high-alloy steels.

(ΔC^O = 0.9 wt%)	low-alloy steel		CF8M steel
	with CO gas	without CO gas	
average inclusion density (g/cm^3)	1.31×10^{-3}	3.23	3.08
average inclusion molecular weight (g/mol)	93	149	83
inclusion mass per mass of oxygen (O) consumed	2.27	1.95	2.30
inclusion moles per mole oxygen (O$_2$) consumed	0.78	0.42	0.89

(a) Visible inclusions, as indicated by circles, on the machined surface of low-alloy steel plates (from Carlson and Beckermann, 2004).

~2 mm
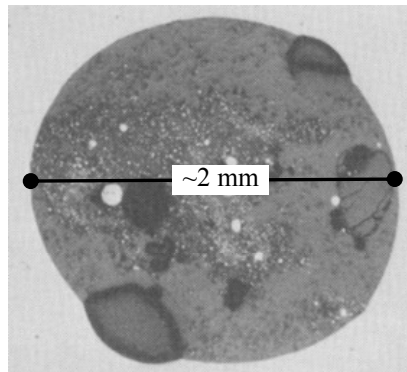
(b) Optical micrograph of a reoxidation inclusion cut from a steel casting; its bulk composition is 34 wt% Al_2O_3, 46 wt% SiO_2, and 20 wt% MnO (from Griffin and Bates, 1991).

Figure 1   Examples of reoxidation inclusions in steel castings.
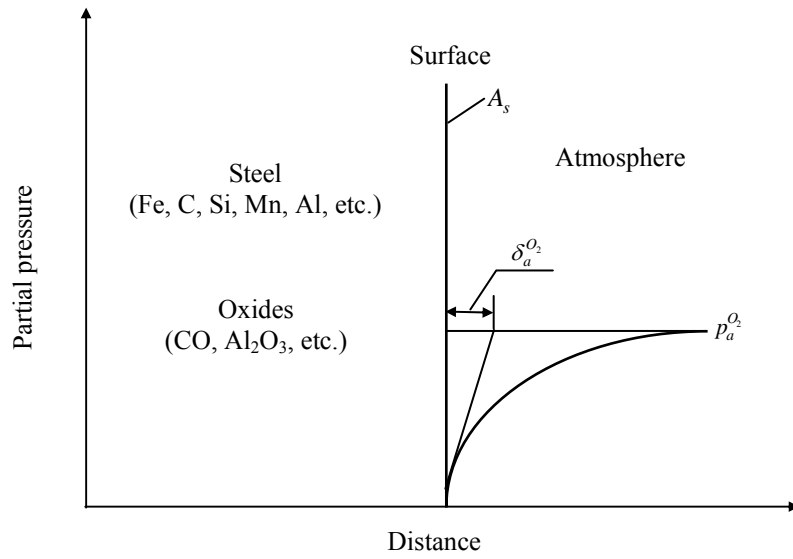
Figure 2 Schematic illustration of oxygen absorption from the atmosphere and the oxygen boundary layer thickness during reoxidation of steel.
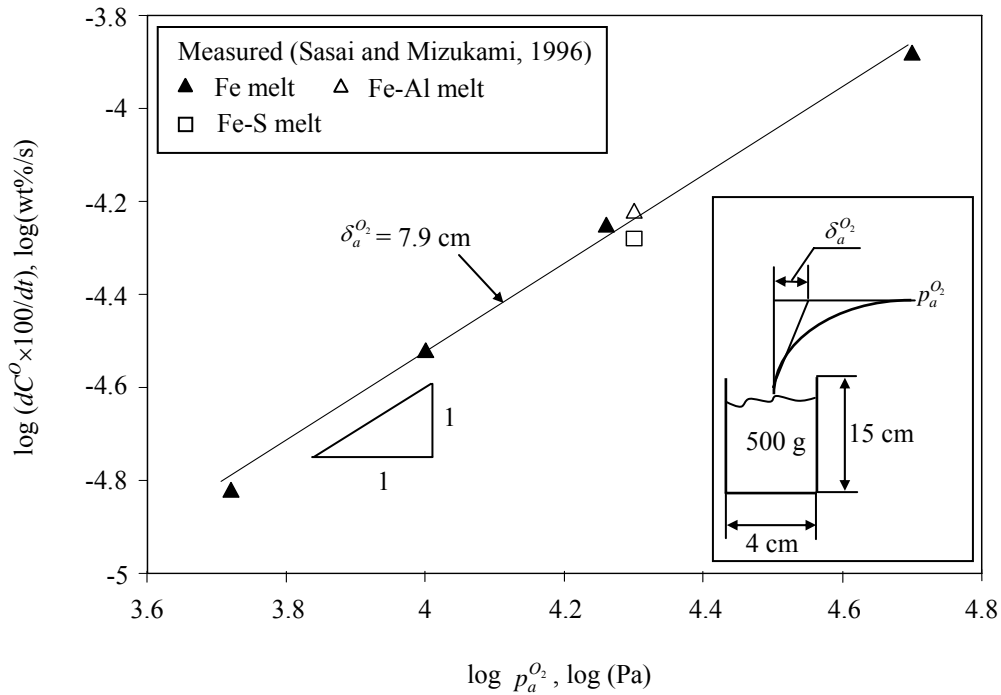
(a) Still state.
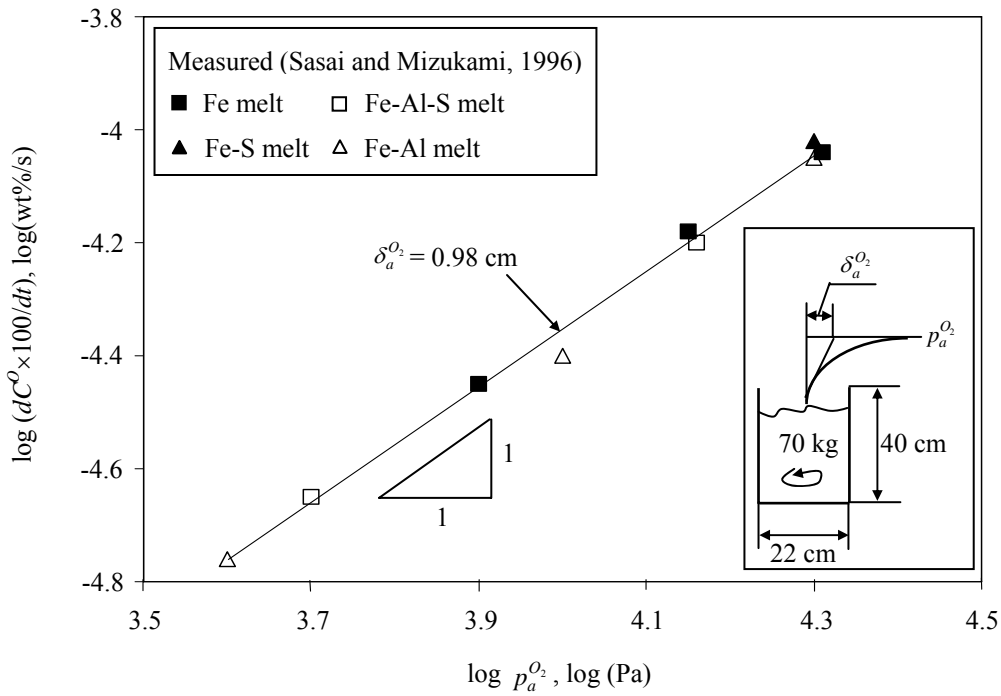
(b) Stirred state.

Figure 3   Variation of the oxygen absorption rate in various Fe melts with the partial pressure of O_2 gas in the atmosphere.
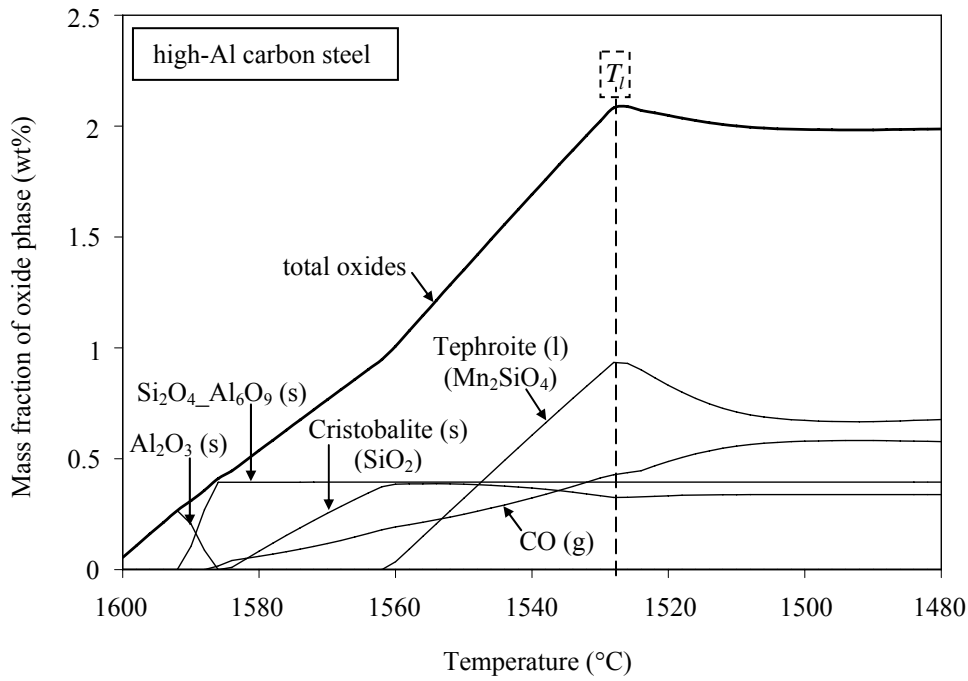
(a) Temperature range: 1600 to 1480 °C.
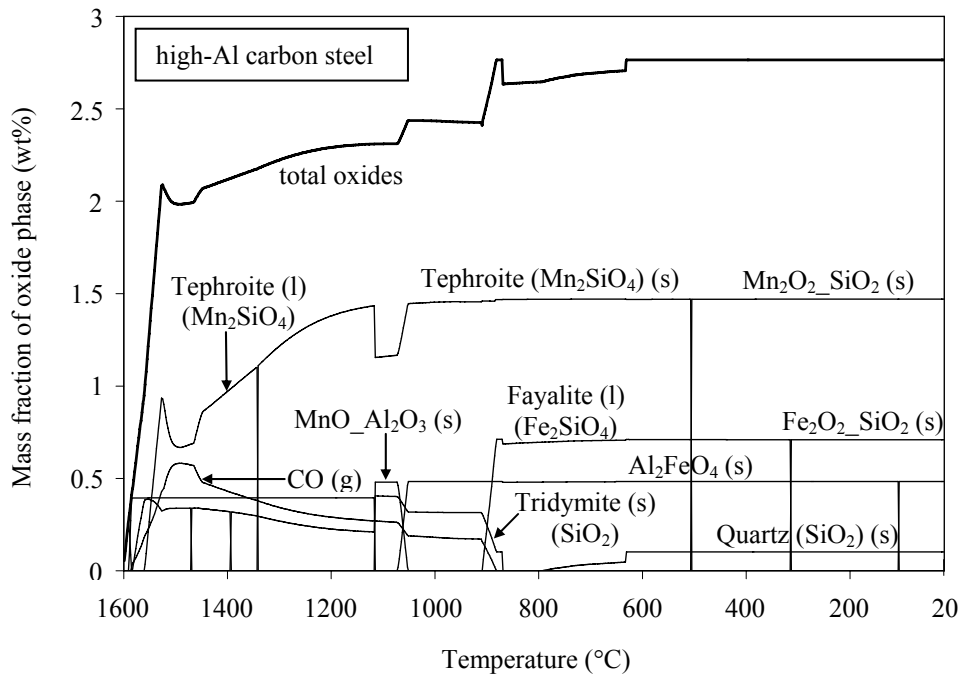
(b) Temperature range: 1600 to 20 °C.

Figure 4   Evolution of the mass fraction of the various oxide phases in high-Al carbon steel calculated using the lever rule method ($\Delta C^O = 0.9$ wt%).
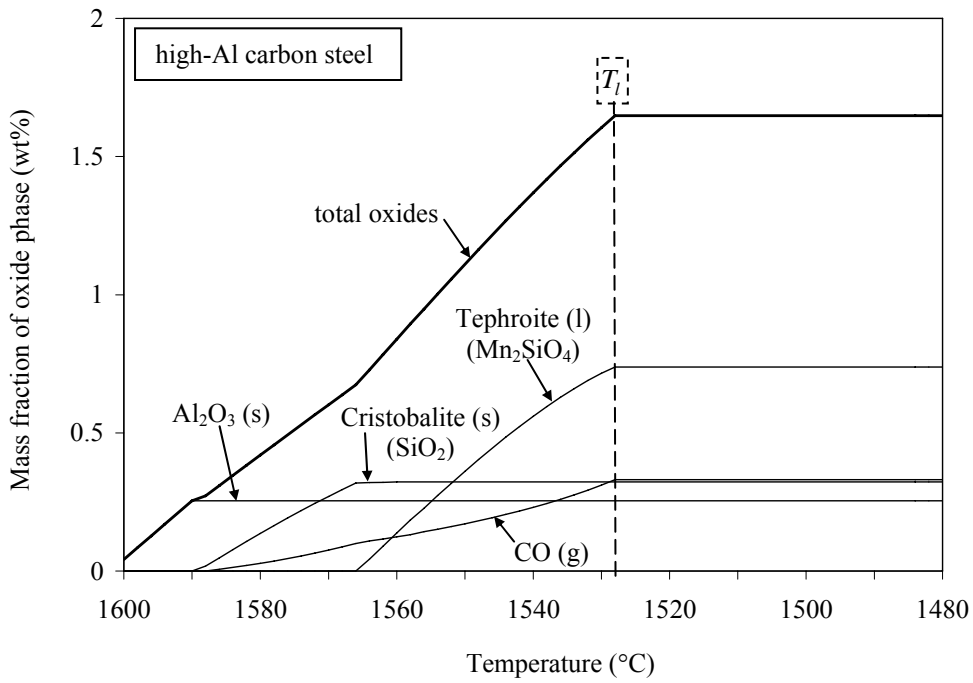
Figure 5 Evolution of the mass fraction of the various oxide phases in high-Al carbon steel calculated using the Scheil method ($\Delta C^O = 0.9$ wt%).
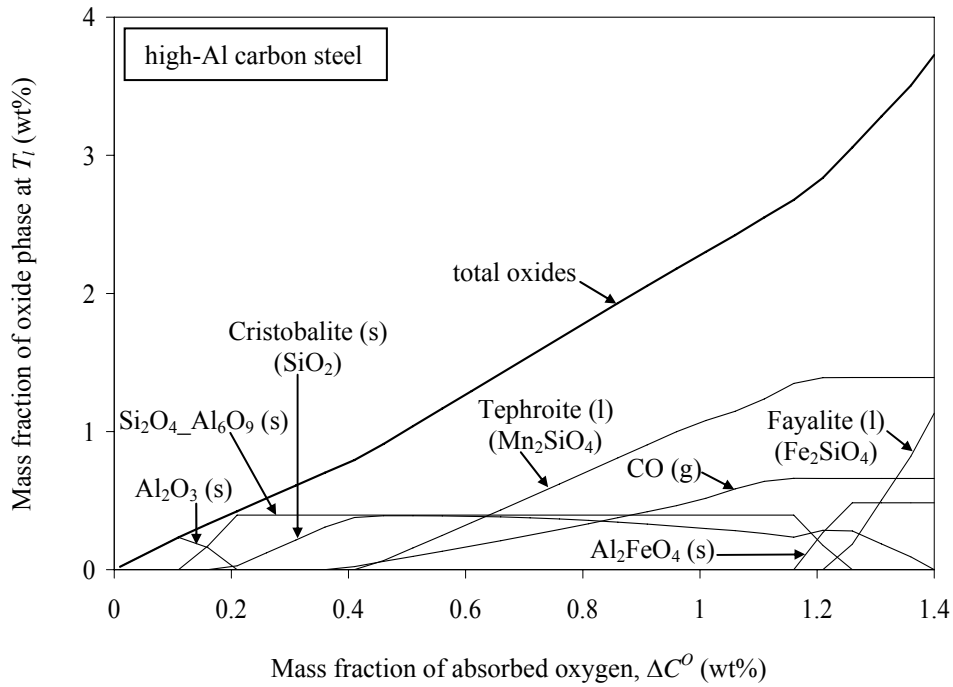
(a) Mass fraction of oxide phases at the liquidus temperature (1528 °C, lever rule).
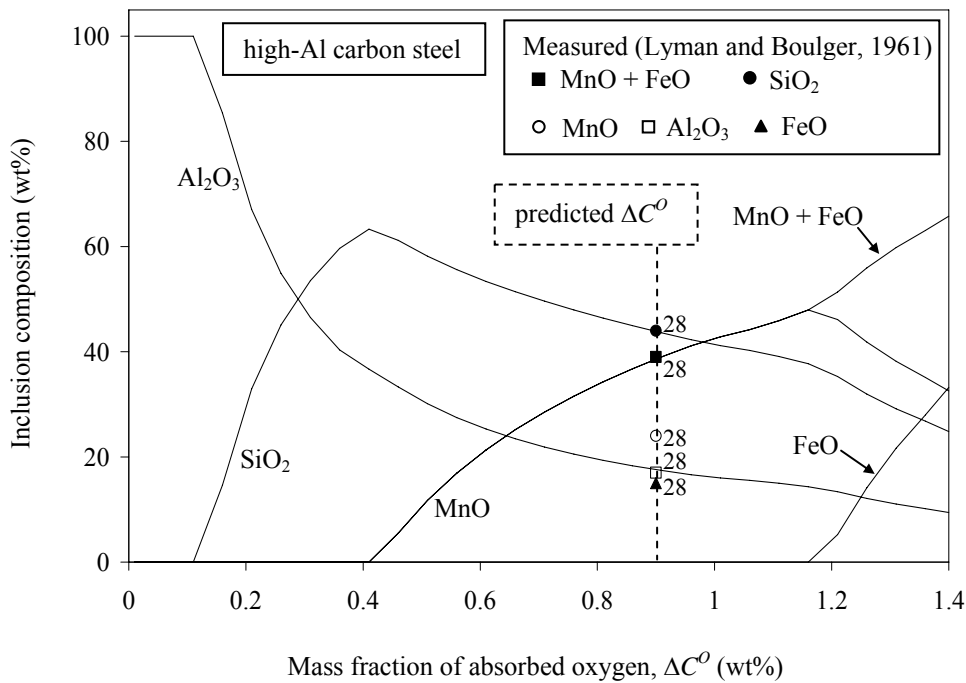
(b) Inclusion composition.

Figure 6 Effect of the mass fraction of absorbed oxygen on the oxide mass fractions at the liquidus temperature and on the inclusion composition for high-Al carbon steel.
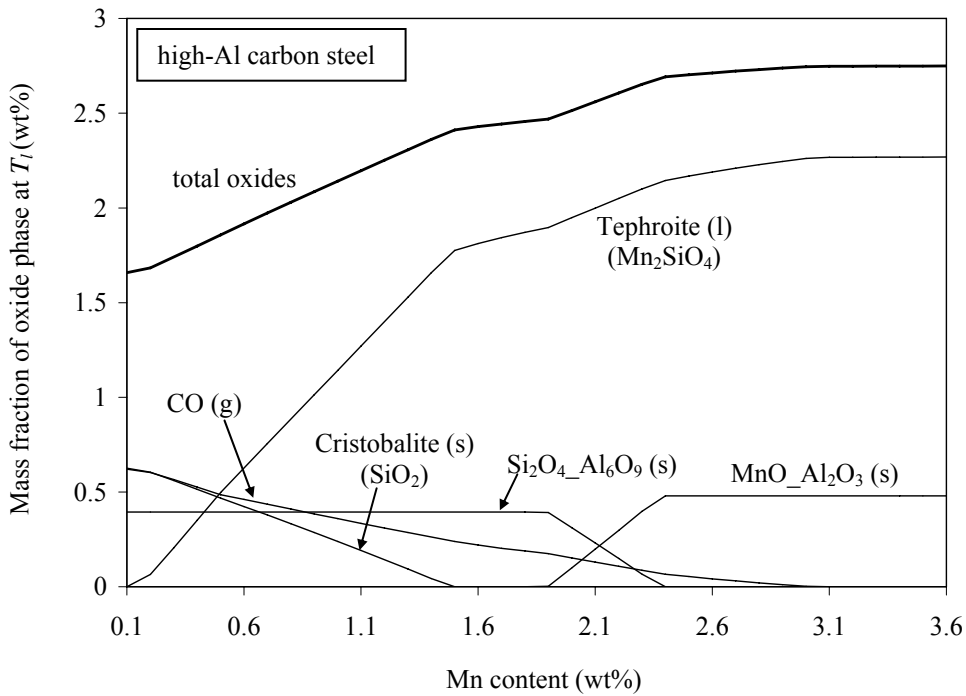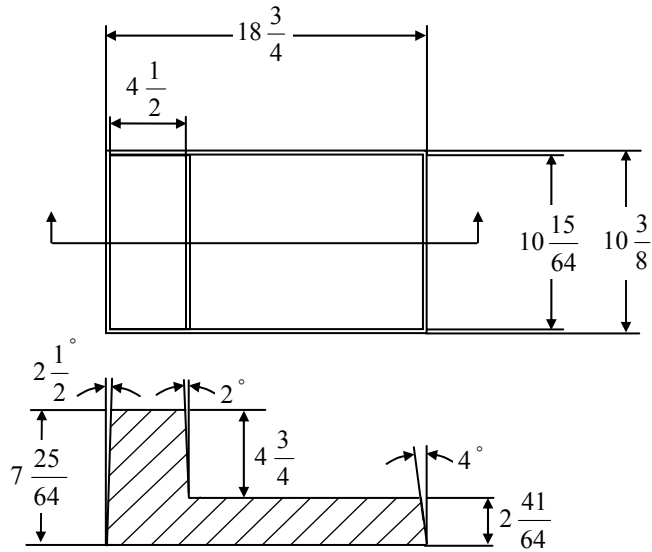
(a) Mass fraction of oxide phases at the liquidus temperature (1528 °C, lever rule).
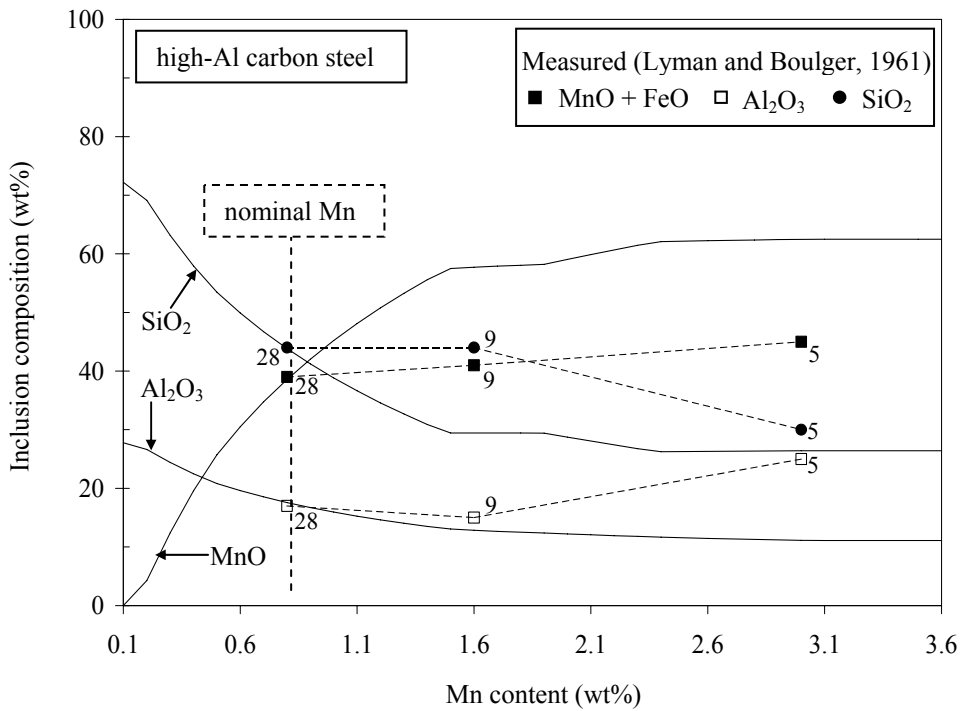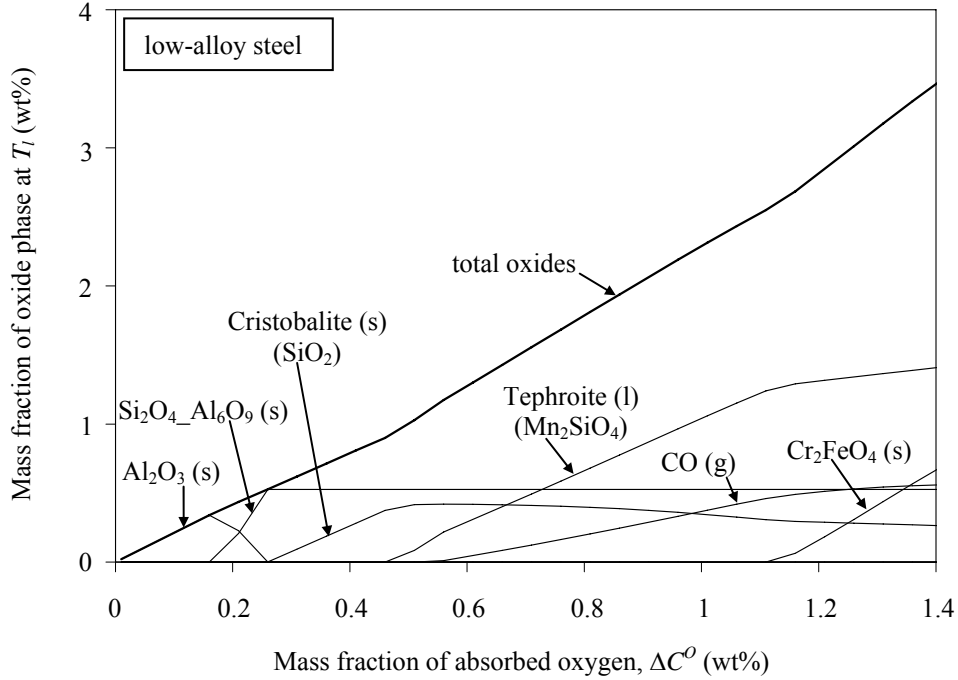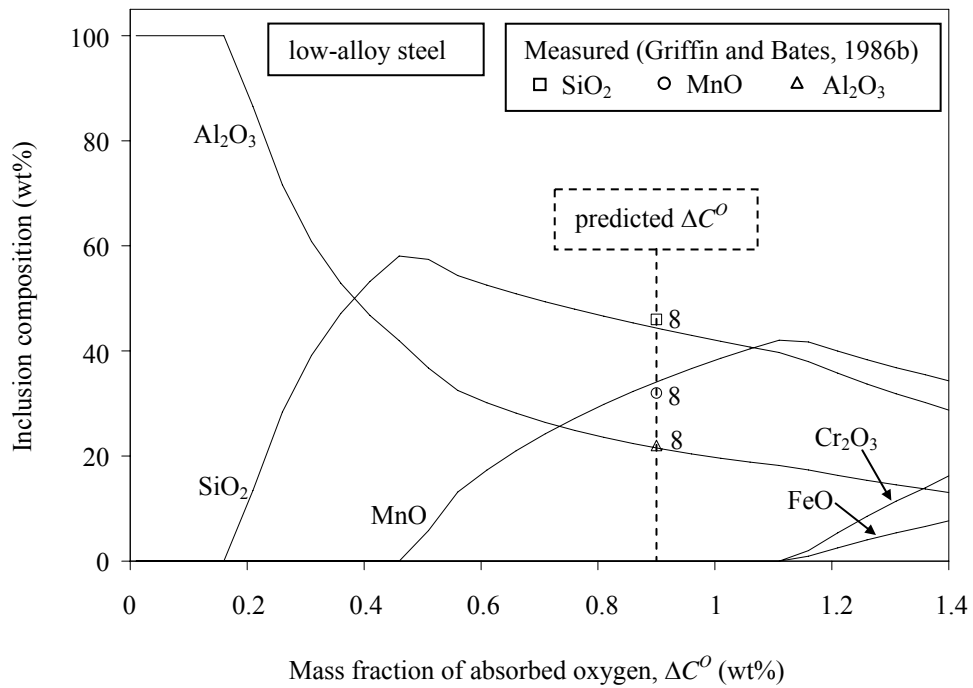

(b) Inclusion composition.

Figure 7   Effect of the Mn content on the oxide mass fractions at the liquidus temperature and on the inclusion composition for high-Al carbon steel ($\Delta C^O = 0.9$ wt%).
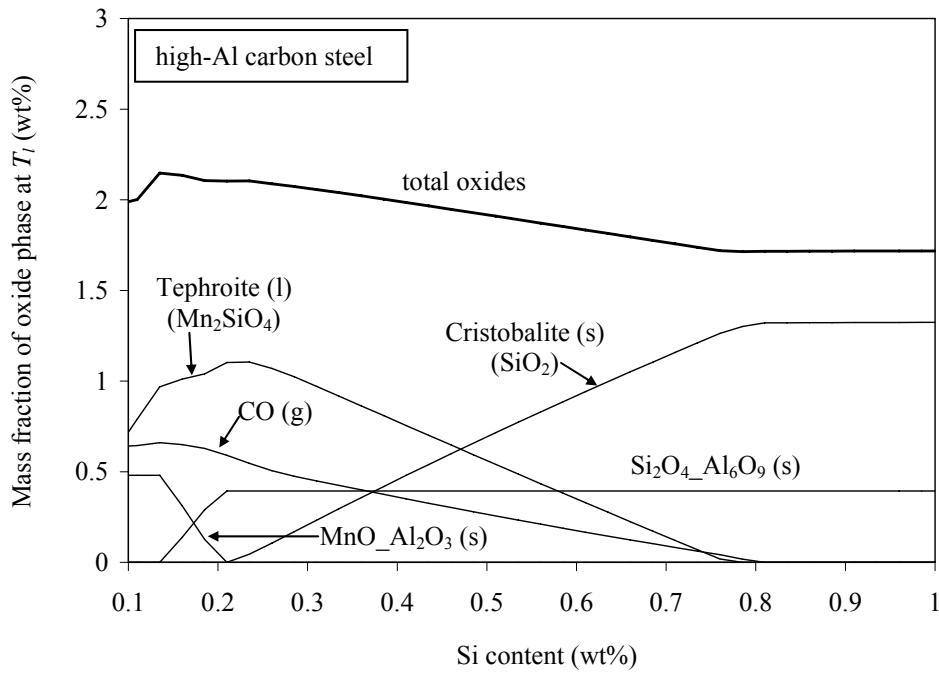
(a) Mass fraction of oxide phases at the liquidus temperature (1528 °C, lever rule).
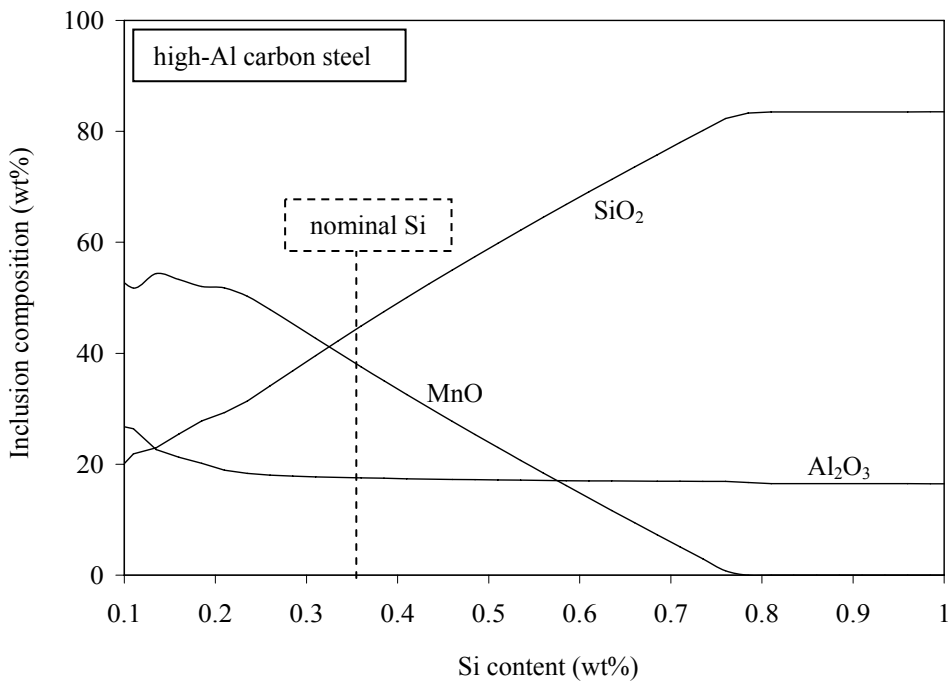
(b) Inclusion composition.

Figure 8   Effect of the Si content on the oxide mass fractions at the liquidus temperature and on the inclusion composition for high-Al carbon steel ($\Delta C^O = 0.9$ wt%).
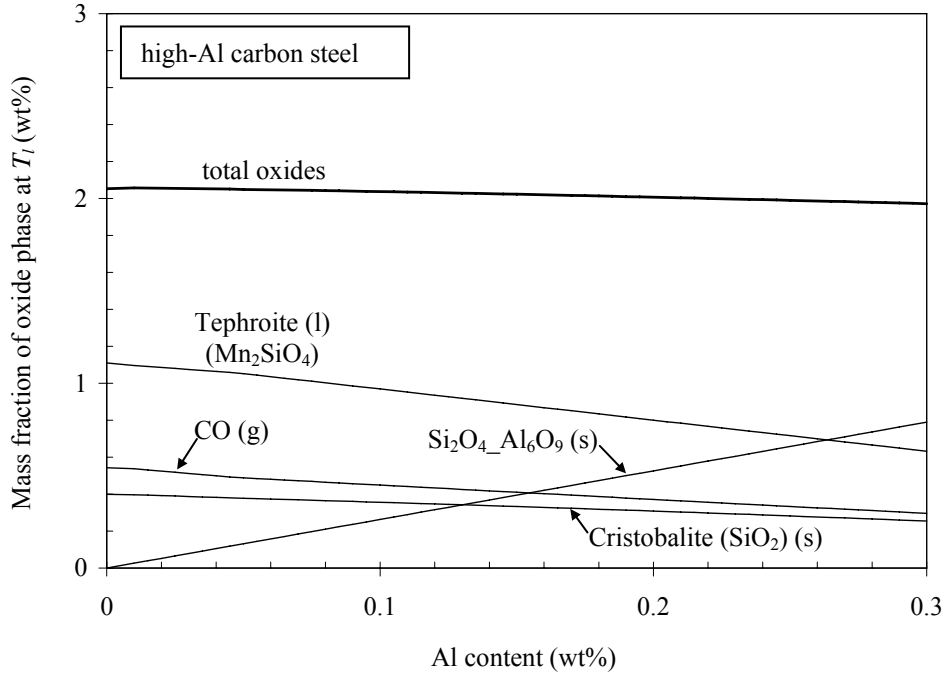
(a) Mass fraction of oxide phases at the liquidus temperature (1528 °C, lever rule).
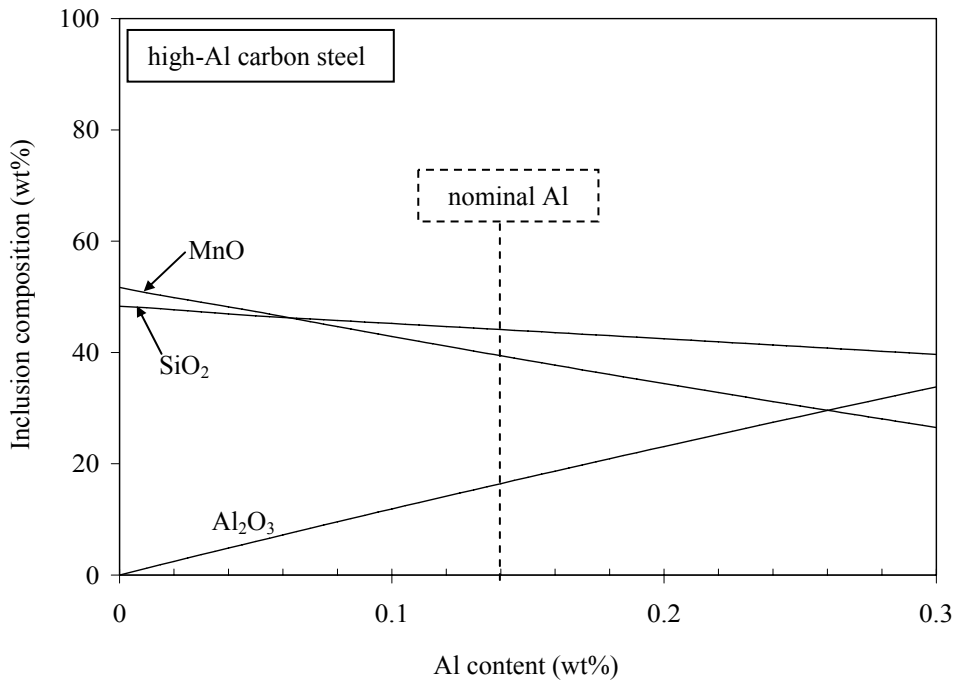

(b) Inclusion composition.

Figure 9 Effect of the Al content on the oxide mass fractions at the liquidus temperature and on the inclusion composition for high-Al carbon steel ($\Delta C^O = 0.9$ wt%).
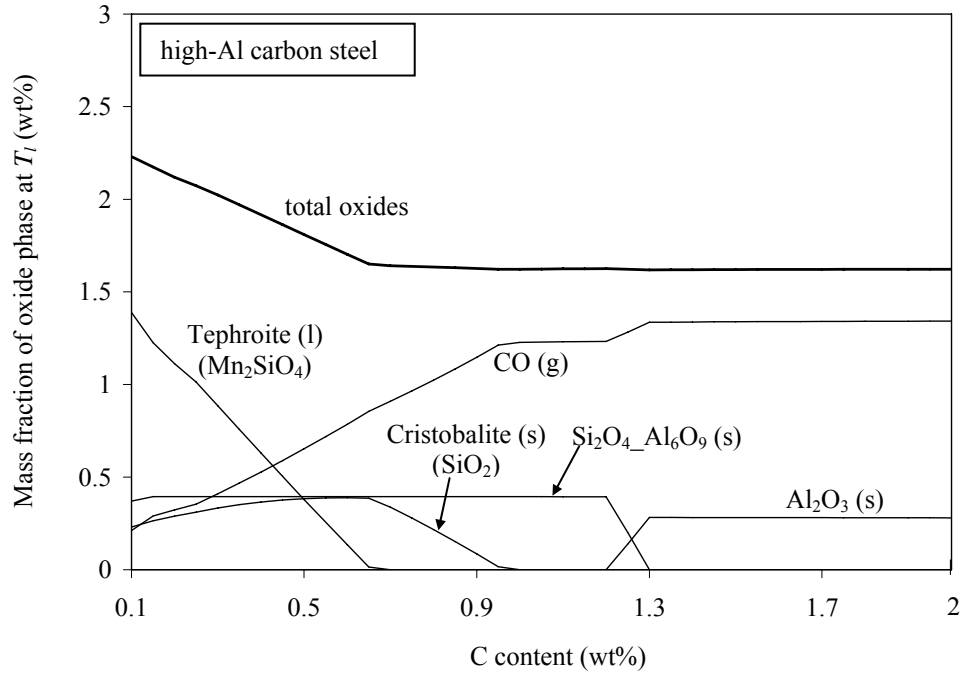
(a) Mass fraction of oxide phases at the liquidus temperature (1528 °C, lever rule).
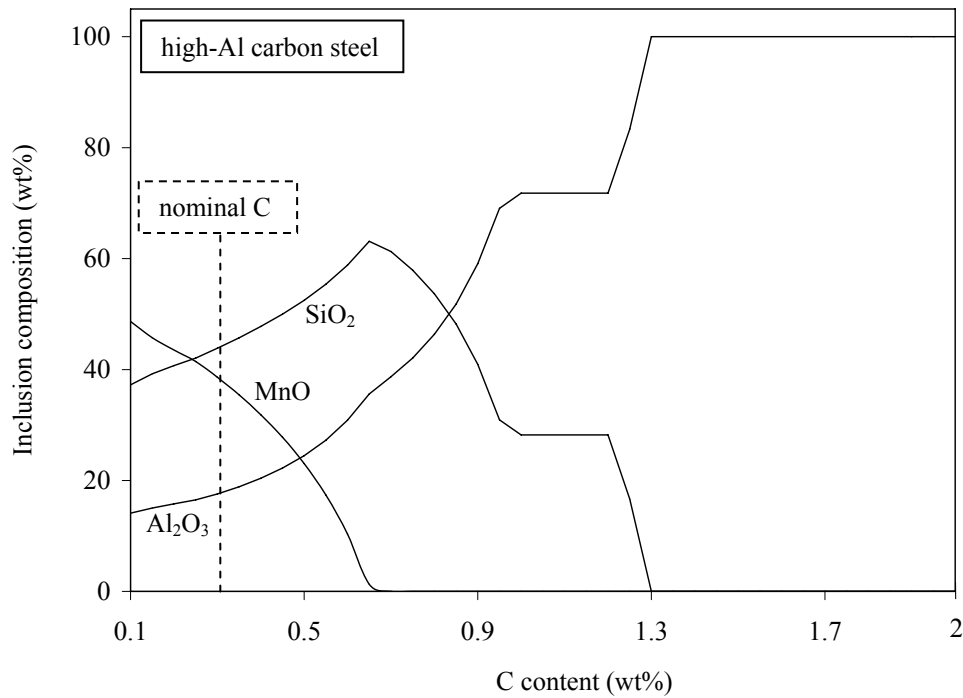
(b) Inclusion composition.

Figure 10 Effect of the C content on the oxide mass fractions at the liquidus temperature and on the inclusion composition for high-Al carbon steel ($\Delta C^O = 0.9$ wt%).
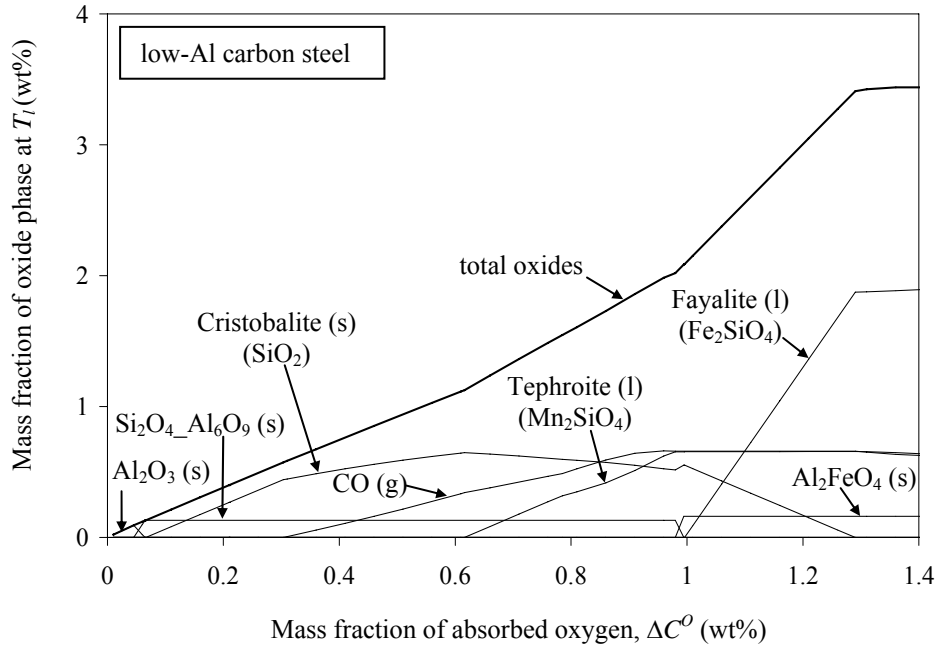
(a) Mass fraction of oxide phases at the liquidus temperature (1528 °C, lever rule).
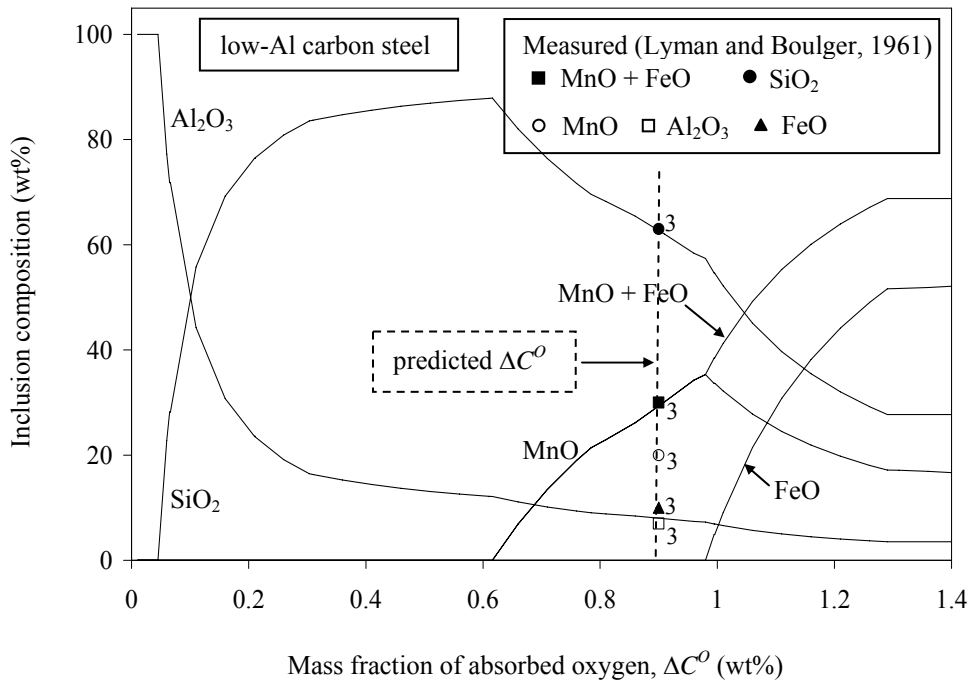
(b) Inclusion composition.

Figure 11 Effect of the mass fraction of absorbed oxygen on the oxide mass fractions at the liquidus temperature and on the inclusion composition for low-Al carbon steel.
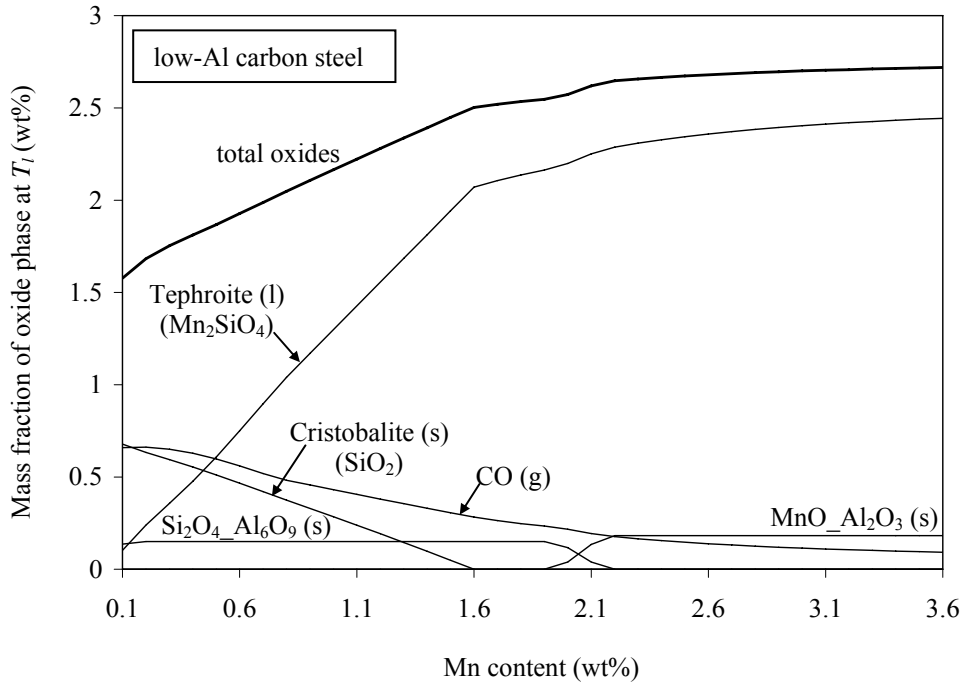
(a) Mass fraction of oxide phases at the liquidus temperature (1528 °C, lever rule).
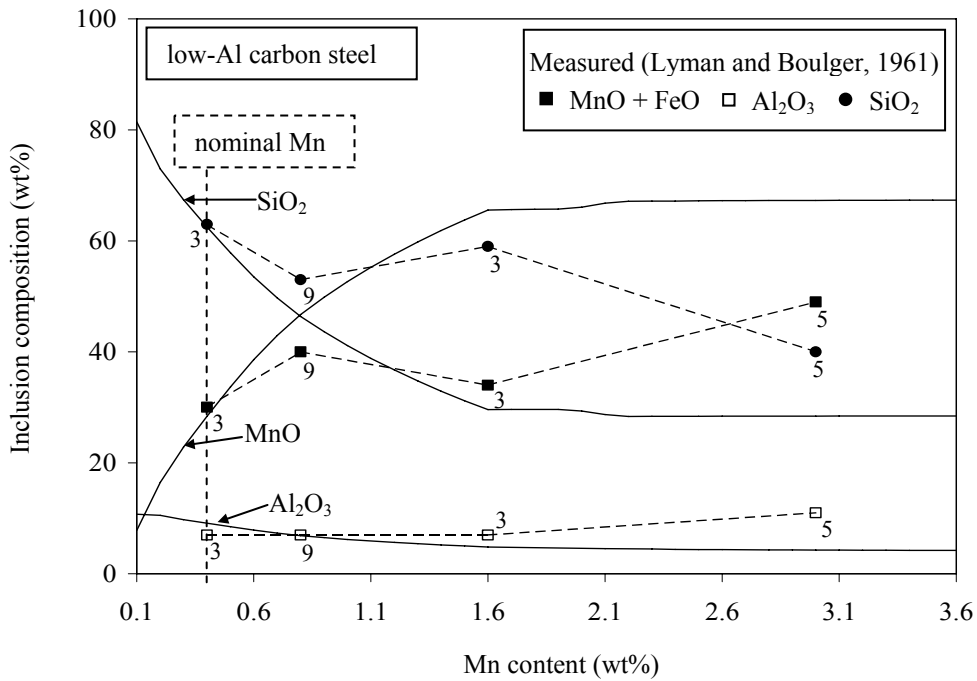
(b) Inclusion composition.

Figure 12 Effect of the Mn content on the oxide mass fractions at the liquidus temperature and on the inclusion composition for low-Al carbon steel ($\Delta C^O = 0.9$ wt%).

Figure 13 Geometry of the low- and high-alloy steel test plate castings (after Griffin and Bates, 1986a and 1986b); the unit for all lengths is inches.

(a) Mass fraction of oxide phases at the liquidus temperature (1528 °C, lever rule).

(b) Inclusion composition.

Figure 14 Effect of the mass fraction of absorbed oxygen on the oxide mass fractions at the liquidus temperature and on the inclusion composition for low-alloy steel.
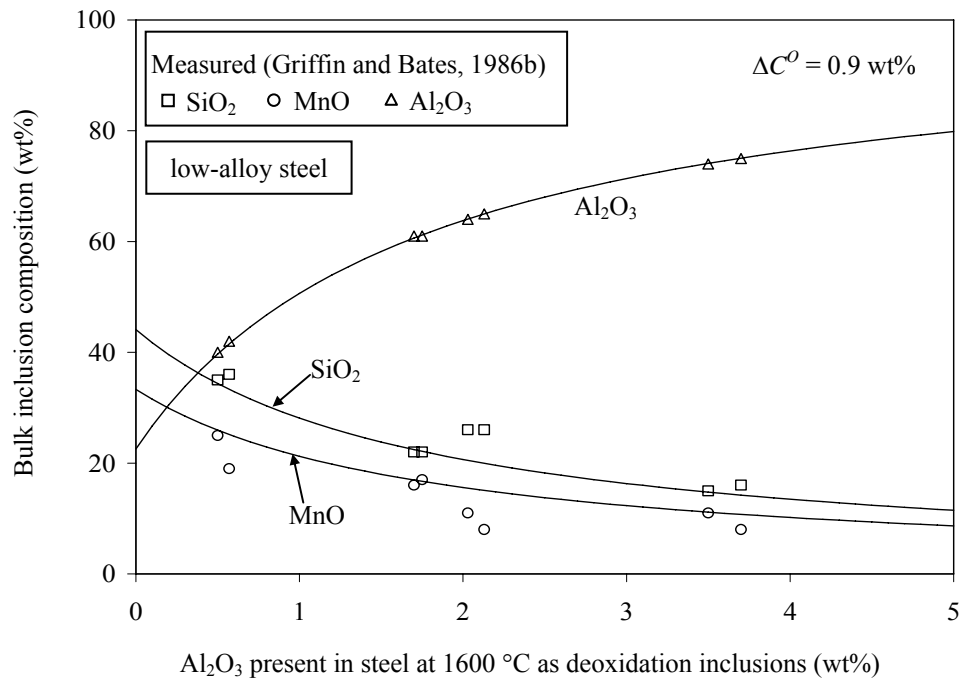
Figure 15 Effect of the mass fraction of Al_2O_3 deoxidation inclusions on the bulk composition of the reoxidation inclusions in low-alloy steel.
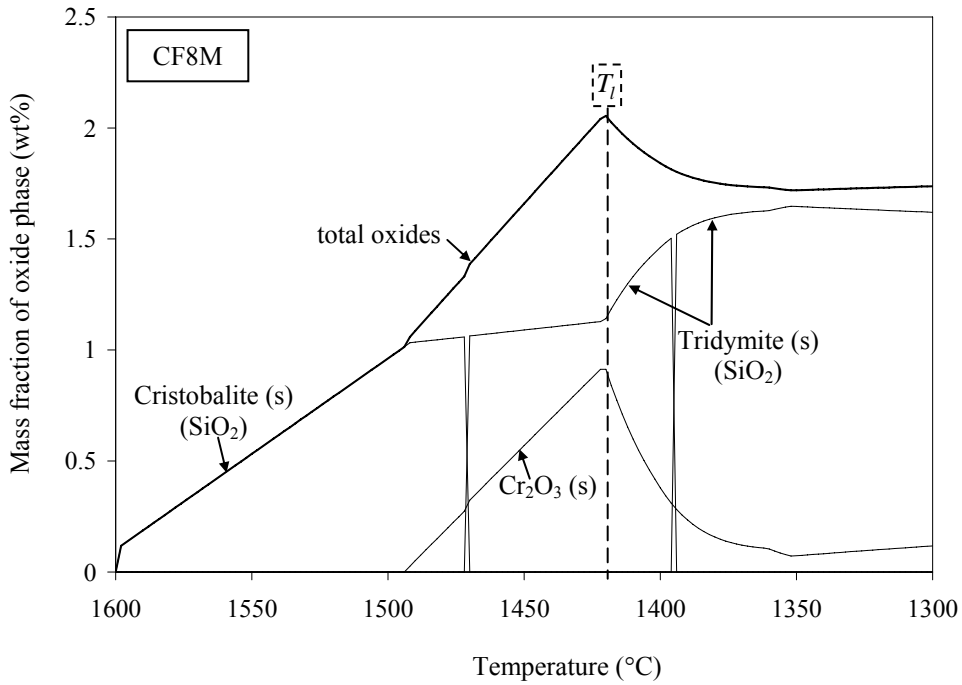
(a) Temperature range: 1600 to 1300 °C.
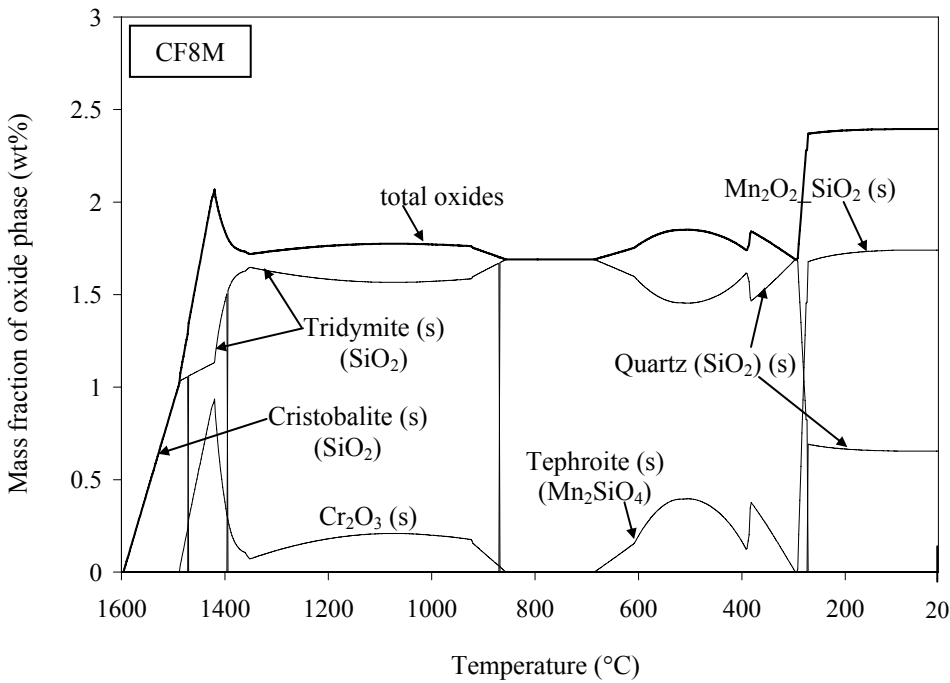
(b) Temperature range: 1600 to 20 °C.

Figure 16 Evolution of the mass fraction of the various oxide phases in high-alloy CF8M steel calculated using the lever rule method ($\Delta C^O = 0.9$ wt%).
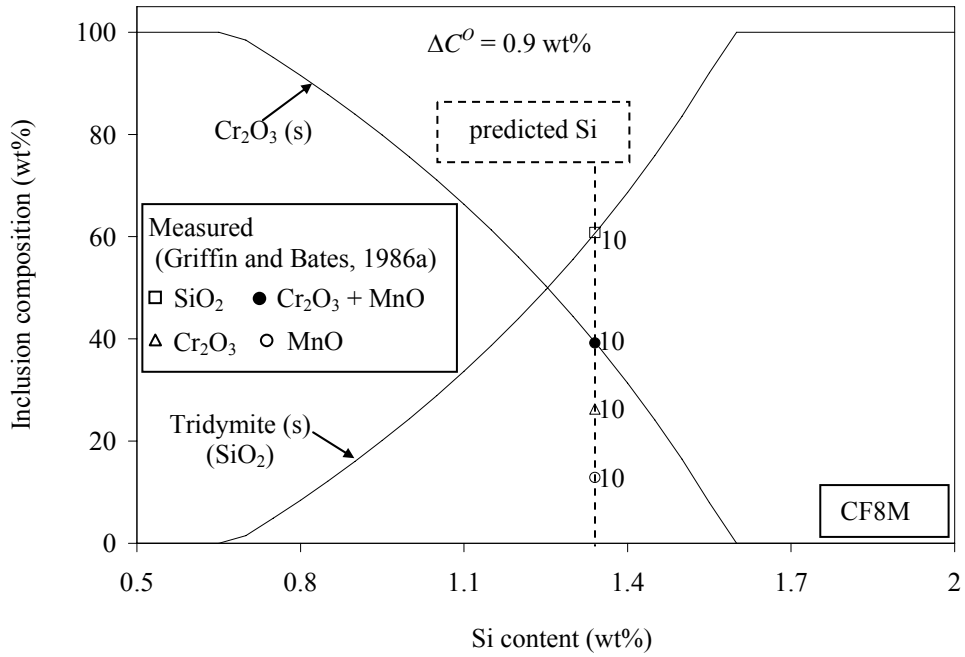
(a) Effect of Si content for $\Delta C^O = 0.9$ wt%.
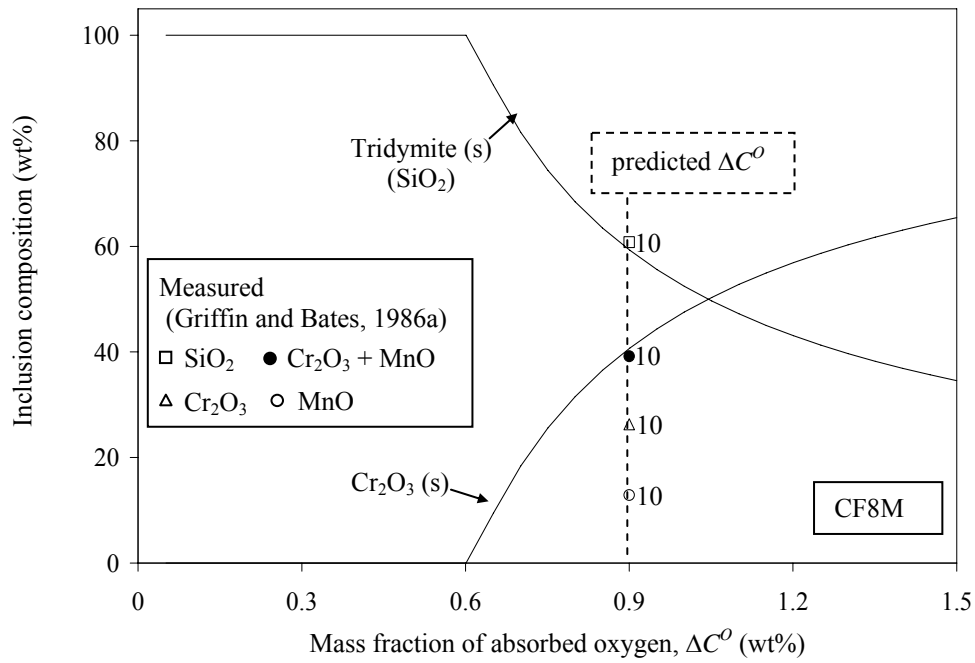
(b) Effect of mass fraction of absorbed oxygen for a Si content of 1.33 wt%.

Figure 17 Effect of the Si content and the mass fraction of absorbed oxygen on the inclusion composition for high-alloy CF8M steel.

46
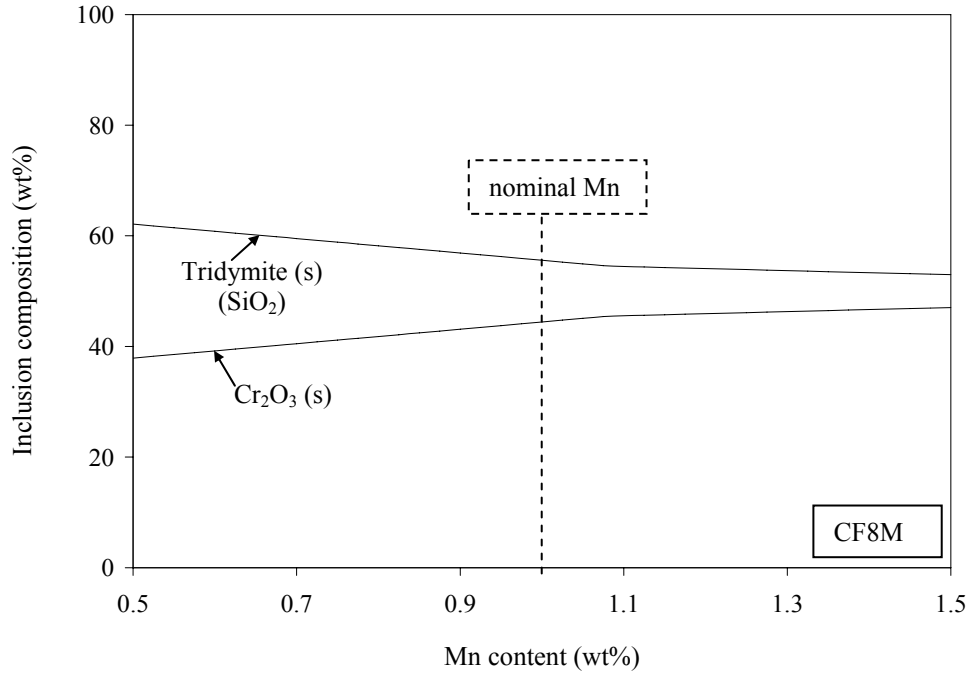
(a) Effect of Mn content.
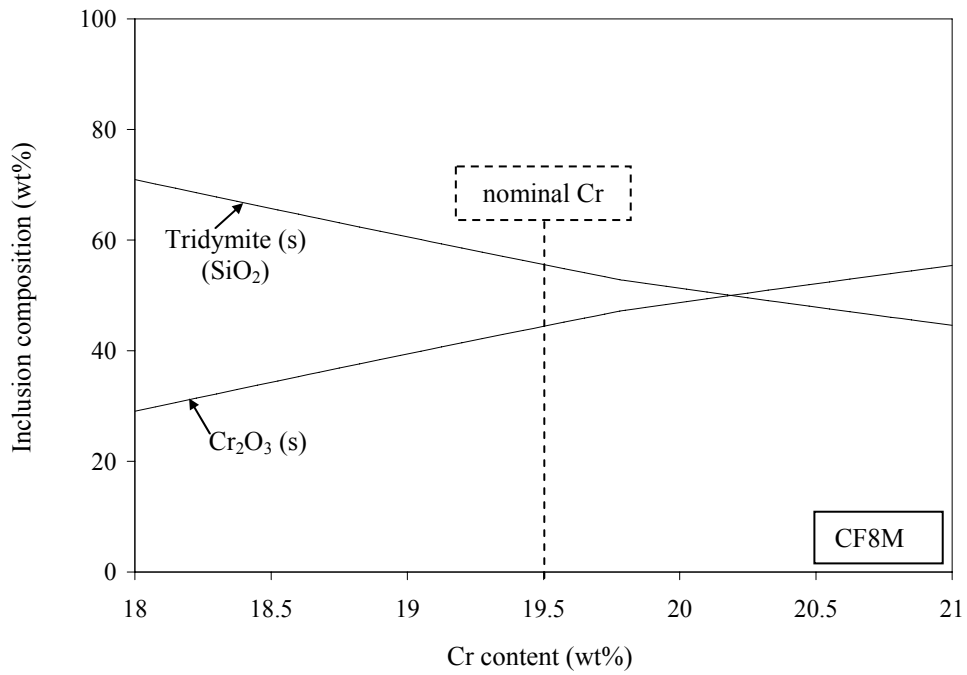
(b) Effect of Cr content.

Figure 18   Effect of the Mn and Cr contents on the inclusion composition for high-alloy CF8M steel ($\Delta C^O = 0.9$ wt%).
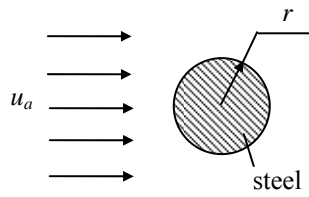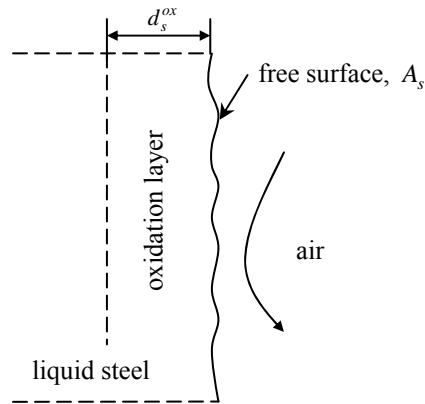
(a) Schematic illustration of air flowing past a steel droplet.
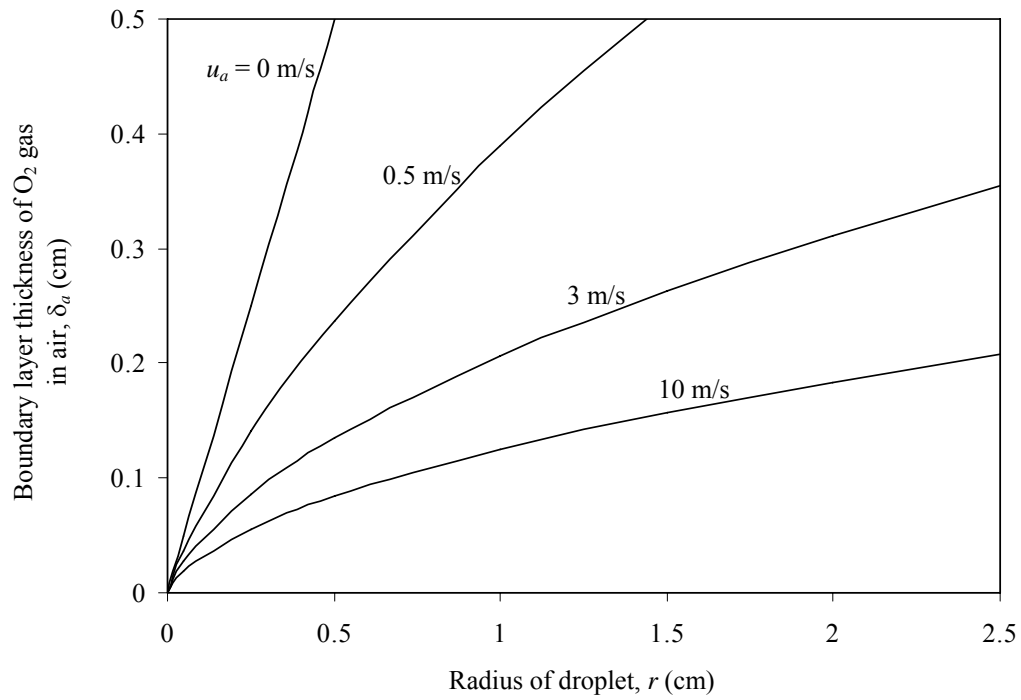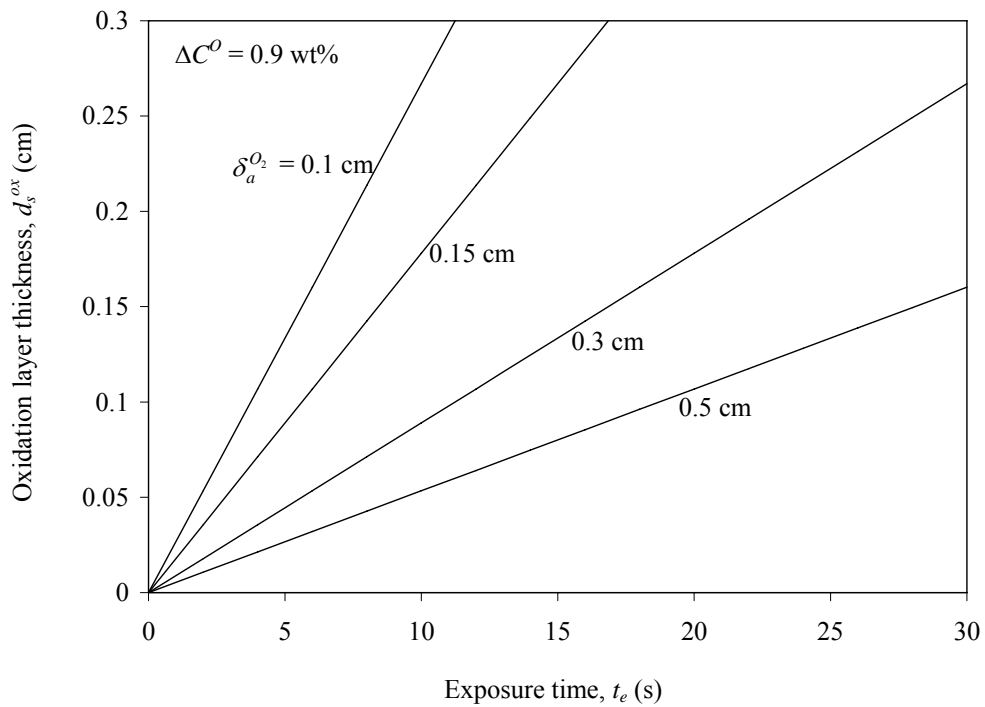

(b) Boundary layer thickness of O_2 gas in air as a function of droplet radius and relative velocity.

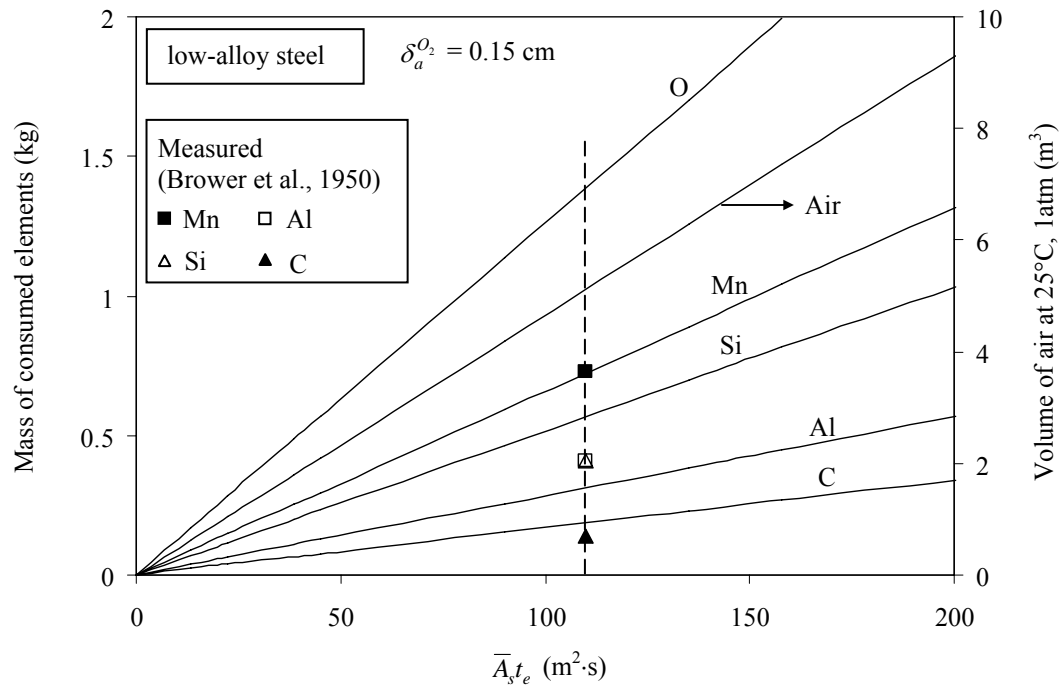**Figure 19** Oxygen transfer from air to a droplet of steel.
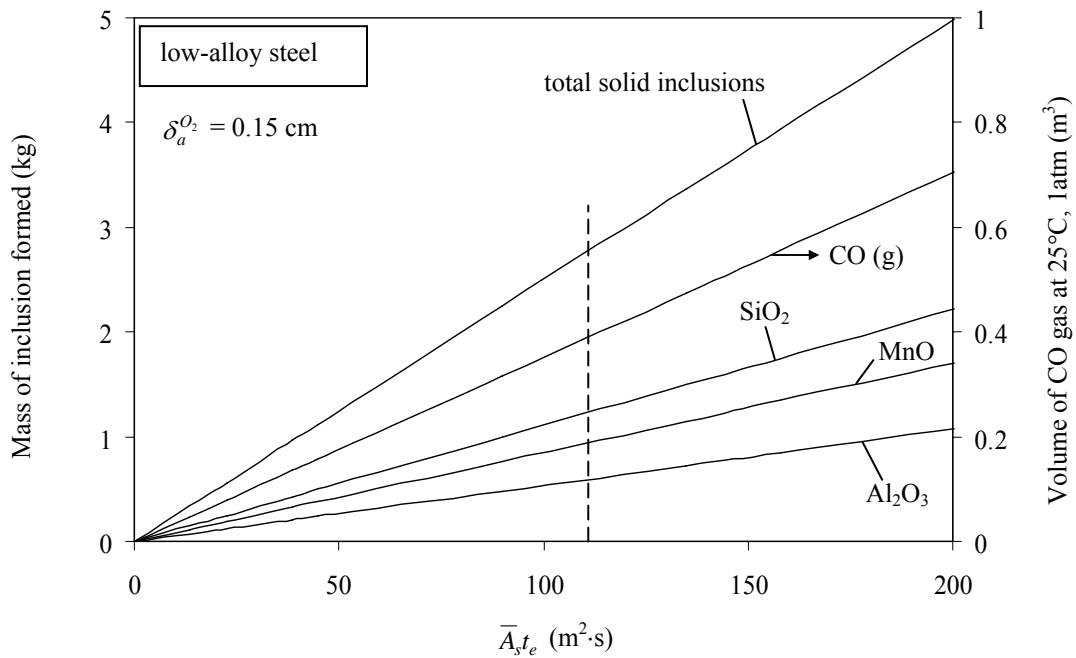
(a) Schematic illustration of the oxidation layer.

(b) Oxidation layer thickness as a function of exposure time and
O$_2$ gas boundary layer thickness.

Figure 20 Oxidation layer adjacent to the free surface of the steel in which the mass fraction of
absorbed oxygen reaches 0.9 wt%.

(a) Mass of consumed alloying elements and volume of air.

(b) Mass of inclusions and volume of CO gas formed.

Figure 21 Mass of consumed alloying elements, volume of air need to supply the oxygen, mass of inclusions formed, and volume of CO gas formed as a function of the integrated free surface area and exposure time product for low-alloy steel ($\delta_a^{O_2} = 0.15$ cm).